FAST REVERSE OSMOSIS THROUGH NANOTUBE-BASED MEMBRANES: MOLECULAR DYNAMICS STUDY

BY

MYUNG EUN SUK

THESIS

Submitted in partial fulfillment of the requirements
for the degree of Master of Science in Mechanical Engineering
in the Graduate College of the
University of Illinois at Urbana-Champaign, 2009

Urbana, Illinois

Adviser:

Professor Narayana R Aluru

Abstract

Development of nanotechnology had led to novel and advanced methods in various fields of science and engineering, and its influence extended to the progress of water purification process. Development of novel membranes and modification of existing membranes for efficient water filtration can be studied based on the investigation of interactions between water and molecules constituting membranes. Also, water molecules confined in nano scale show different behavior from the bulk water, and the study of this behavior can contribute to enhance water flux and energy efficiency. Molecular dynamics simulation can be used in observing these features that experiments can not detect. In this work, we performed molecular dynamics simulation to investigate the methods to improve reverse osmosis process, which can produce high quality water by removing ions and emerging pollutants.

In the first part, we investigate reverse-osmosis through commonly used polymeric and advanced inorganic nanotube based semi-permeable membranes by performing non-equilibrium molecular dynamics simulations. Simulations indicate that there is a significantly higher water flux through boron nitride (BNNT) and carbon nanotubes (CNT) compared to a polymethyl methacrylate (PMMA) pore, and a slightly higher water flux through BNNT as compared to CNT. The calculated permeation coefficient is in reasonable agreement with the theoretical single-file "hopping" model. Potential of mean force analysis indicates that the irregular nature of PMMA pore surface can cause significant localized energy barriers inside the pore, thereby reducing the water flux.

In the second part, we investigated the effect of electric field on single-file reverse osmosis (RO) water flux. The electric field is generated by introducing oppositely charged

biomolecules to the salt solution and pure water chambers attached to the nanopore. Simulation results indicate that an electric field in the direction of RO enhances the water flux while in the direction opposite to RO suppresses the water flux. When the RO water flux is enhanced, the single-file water dipoles are aligned in the direction of the electric field. The addition of an electric field in the direction of RO led to a flux of 3 water molecules/ns by constantly maintaining water dipole vectors in the direction of electric field, and this water flux is superimposed on the pressure driven water flux.

Acknowledgments

This project would not have been possible without the support of many people. I would like to thank my advisor, Narayan Aluru, for his patience, constant guidance, and encouragement with my research. I would also like to thank my mentor, Anjan Raghunathan, for his advice and care. Also, thanks to graduate students in the Computational MEMS/Nanotechnology group for their helpful discussion. Thanks to my family who always offer support and love. Finally, I would like to acknowledge the support of this work by the WaterCAMPWS Science and Technology Center under National Science Foundation Agreement Number CTS-0120978.

Table of Contents

Chapter 1

Introduction

Nanotechnology, which deals with systems and devices at the nano scale regime is currently being used in various fields of study. The fields of study covers most engineering and science fields and is already being used in our everyday lives. Nanofluidics deals with fluid transport in nanometer scale channels and pores, which is especially important in drug delivery, membrane separation, lap-on-a-chip devices, and so forth. In nanofluidics, molecular dimensions or mean free path of molecules are similar to channel dimensions, which causes different behavior from the fluid dynamics on a micro or macro scale. On macro scales, collisions between molecules are much larger than the collisions between molecules and channel walls while they are comparable to each other in nano scale channels.Experiments on nanofluidics is challenging because of fabrication of nanofluidics devices and observation and measurements of fluids at nano scale. In this situation, molecular dynamics simulation is an useful tool in studying nanofluidics.

As nanotechnology is studied in various fields, molecular dynamics simulation is used as a useful tool. Usually, molecular dynamics simulation is interpreted as an experiment using computer, or the middle state between theory and experiment. Due to the development of computers and increase in computer speed, time scale of molecular dynamics simulation has been extended, and most properties obtained in macro scale experiments are available using molecular dynamics simulation. Dynamic as well as static properties of fluids in nano scale pore can be extracted using molecular dynamics simulation. Also, fluid behavior in nano scale pore can be observed on a molecular level. Thus, molecular dynamics simulation is a powerful tool in studying nanofluidics.

As mentioned earlier, one of the fields related to nanofluidics is membrane separation technology. Membrane separation technology ranges from particle filtration to reverse osmosis depending on pore sizes of membranes, and can separate various sizes of molecules using such membranes. The applications of membrane separation include bio-separation, water purification, and so on. Reverse osmosis is used in producing potable water from the seawater since it can remove ions and most of all contaminants. However, reverse osmosis is the most expensive process energetically speaking.

In this thesis, we focused on studying effective water filtration using reverse osmosis due to the importance of water purification. Water shortage is a global issue that requires concerted efforts from not only developing countries, which are currently suffering from water shortage, but also developed countries. In fact, various scientific and engineering fields have contributed to and paid attention to the study of effective water purification by desalination or waste water treatment [1]. In particular, the significance of desalination can be found from the fact that the largest water sources are seawater and saline aquifers, which composed 95% of water on earth [1]. Our work studied reverse osmosis membrane and process that can reduce the energetic cost of desalination by using molecular dynamics simulation. Further motivation and background can be found in introductory sections of chapter 3 and chapter 4.

The thesis is organized as follows. A brief overview of the MD simulations and some implementation details of MD methodologies are given in chapter 2. Simulation set-up and methods of reverse osmosis are also given in the last section of chapter 2. In chapter 3, we studied reverse osmosis through advanced nanotube membranes and polymeric membranes. Chapter 3 includes an introduction, membrane preparation, results and analysis, and conclusions. In chapter 4, we studied the effect of an induced electric field on reverse osmosis. Chapter 4 includes an introduction, method to induce an electric field, simulation details, results and analysis, and conclusions. Finally, the conclusions of the thesis is presented in chapter 5.

Chapter 2

Molecular dynamics simulation of reverse-osmosis

2.1 Overview of molecular dynamics simulation

Molecular dynamics (MD) simulation calculates interatomic forces acting on each atom in the system, and integrates Newton's equations of motion to find molecular *trajectories*, and coordinates of atoms as a function of time. From molecular trajectories, dynamic as well as static properties can be extracted to analyze simulation results.

The interatomic forces can be obtained by taking the derivative of the potential energy expressed as follows [2]:

$$\mathbf{F_i} = -\frac{\partial U}{\partial \mathbf{r_i}}, i = 1, 2, \cdots, N \tag{2.1}$$

where $\mathbf{F_i}$ is the force acting on i_{th} atom, $\mathbf{r_i}$ is position of i_{th} atom, N is the total number of atoms in system, and U is the potential energy. Potential energy, U, is given by

$$U = \sum_i u_1(\mathbf{r_i}) + \sum_i \sum_{j>i} u_2(\mathbf{r_i}, \mathbf{r_j}) + \sum_i \sum_{j>i} \sum_{k>j>i} u_3(\mathbf{r_i}, \mathbf{r_j}, \mathbf{r_k}) + \dots \tag{2.2}$$

where, u_1 is the potential energy due to external field, u_2 is pairwise potential, and u_3 is three body potnetial, etc. Newton's equation of motion,

$$\mathbf{F_i} = -\frac{\partial^2 \mathbf{r_i}}{\partial t^2}, i = 1, 2 \cdots, N \tag{2.3}$$

is numerically integrated to find molecular trajectories, $\mathbf{r}(t)$. The general MD algorithm is

summarized in Table 2.1.

Table 2.1: General MD algorithm

	MD algorithm
1:	Input parameters:
	Force field, time step, ensemble, etc..
2:	Input initial conditions
	Positions, $\mathbf{r_i}$ and velocities, $\mathbf{v_i}$ of all atoms in system
	Repeat 3∼6 for required time steps:
3:	Compute force on any atom based on input potential
4:	Integrate Newton's equation of motion
5:	Update configuration
6:	If necessary, write positions, velocities, energy, etc.

2.2 Interatomic potential

Accuracy and computational efficiency is essential in selecting interatomic potential. The potential function can be divided into three parts: non-bonded, bonded, and restraints.

Non-bonded interaction

Lennard-Jones (LJ) potential is widely used for non-bonded, van der Waals interaction. LJ potential is pairwise and additive, which can be written as:

$$U_{LJ}(r_{ij}) = 4\varepsilon_{ij}((\frac{\sigma_{ij}}{r_{ij}})^{12} - (\frac{\sigma_{ij}}{r_{ij}})^{6}) \tag{2.4}$$

where ε_{ij} and σ_{ij} are LJ parameters for interacting atoms. ε_{ij} represents depth of potential well and σ_{ij} represents finite distance between atoms at which the potential is zero. Since LJ potential is short range interaction, cut-off scheme can be used to reduce computational expense without introducing a significant error.

For charged and non-bonded particles, electrostatic interaction (Coulomb interaction) is

expressed as:

$$U_c(r_{ij}) = \frac{1}{4\pi\epsilon_0}\frac{q_i q_j}{\epsilon_r r_{ij}} \tag{2.5}$$

where ϵ_0 is permittivity of vacuum, ϵ_r is the relative permittivity, and q_i and q_j are charges on atoms i and j, respectively. Since Coulomb interaction is long range, cut-off scheme used for LJ potential causes significant error in calculating electrostatic potential. Besides, calculation of entire Coulomb interaction causes significant computational expense, especially when periodic boundary condition is applied. To solve this problem, Ewald summation providing relative accuracy and efficiency was developed. Details on Ewald summation and correction for reduced periodicity will be discussed in the next section.

Bonded interaction

Bonded interactions include 3- and 4-body interactions as well as pair interactions. *B stretching*, *bond angle*, and *dihedral angle* are pair, 3-body, and 4-body interactions, respectively. Bond stretching associated with vibrations along covalent chemical bonds can be expressed by harmonic potential given by

$$U_b(r_{ij}) = \frac{1}{2}k^b_{ij}(r_{ij} - b_{ij})^2 \tag{2.6}$$

where k^b_{ij} is force constant that gives stiffness of bond, and b_{ij} is equilibrium bond length. Anharmonic bond stretching potential such as Morse potential and cubic bond stretching potential are also available.

Bond angle associated with bending motion between two adjacent bonds is also expressed as harmonic potential on the angle Θ_{ijk}, angle between atom i-j bond and atom j-k bond.

$$U_a(\theta_{ijk}) = \frac{1}{2}k^\theta_{ijk}(\theta_{ijk} - \theta^0_{ijk})^2 \tag{2.7}$$

where k_{ijk} is force constant and θ^0_{ijk} is equilibrium bond angle.

Dihedral angle associated with the torsional motion is assumed to be periodic and is often expressed as cosine function.

$$U_d(\phi_{ijkl}) = k_\phi(1 + cos(n\phi_{ijkl} - \phi_s)) \tag{2.8}$$

where ϕ_{ijkl} is the angle between plane containing i,j,k atoms and j,k,l atoms k_ϕ is rotational force constant, n is the number of maxima (or minima) in one full rotation, and ϕ_s is the angular offset. Other forms such as harmonic, combined harmonic and cosine function are also available. Parameters introduced in potential function varies with atom types. Potential functions and parameters derived from experiment or high-level quantum mechanical calculations are available in various force fields such as GROMOS, Amber, CHARMM, OPLS-AA, MMFF, MM2, etc.

2.3 Long range electrostatics

Short range LJ interaction is easily calculated using cut-off scheme, and is computationally inexpensive. Calculating long range interaction, such as electrostatic interaction, can not be accurately calculated using cut-off scheme. Thus, efficient technique which can accurately calculate long range interaction and save computational time is necessary. Various techniques such as Ewald summation, Fast multipole methods and particle-mesh-based-techniques are developed [3]. Computational time for Ewald summation is $0(N^3/2)$. To save the computational time for large system, Particle-particle/particle-mesh [4] method which scales as 0(NlogN), and Fast multipole method [5] which scales as 0(N) have been developed. However, Fast multipole method is efficient for systems having more than 10^5 particles. Particle-mesh Ewald summation is an attractive method for systems having $10^3 \sim 10^4$ particles.

Ewald summation

Electrostatic potential introduced in the previous section can be rewritten by the following equations for a system having N particles and periodic box size L,

$$U_c = \frac{1}{2}\sum_{i=1}^{N} q_i \phi(r_i) \tag{2.9}$$

where

$$\phi(r_i) = \Sigma'_{j,\mathbf{n}} \frac{q_j}{|\mathbf{r}_{ij} + \mathbf{n}L|} \tag{2.10}$$

$\mathbf{n}$ is the three-dimensional integer vector representing periodic images. The sum is over all particles j and periodic images $\mathbf{n}$ except $j = i$ if $\mathbf{n} = (0, 0, 0)$. Thus, particle i interacts with all other particles, j, except particle, i, itself and all periodic images of particles.

Since the above summation converges poorly, Fourier space can be used to improve the convergence. Each point charge can be screened using a diffuse cloud of opposite charge around each point charge, and then it can be compensated using a smoothly varying periodic charge density. Electrostatic potential due to screened point charge rapidly goes to 0 at large distances, and it can be treated with real space cut-off scheme. The compensating charge density is treated with Fourier space. Screening charge density can be expressed using Gaussian distribution:

$$\rho(r) = -q_i(\alpha/\pi)^{(3/2)} \exp(-\alpha r^2) \tag{2.11}$$

Periodic sum of Gaussian distributions is given by

$$\rho(r) = \sum_{j=1}^{N}\sum_{n} q_j(\alpha/\pi)^{(\frac{3}{2})} \exp[-\alpha|\mathbf{r} - (\mathbf{r}_j + \mathbf{n}L)|^2] \tag{2.12}$$

Poisson's equation can be used to obtain potential energy given by

$$-\nabla^2\Phi(\mathbf{r}) = 4\pi\rho(\mathbf{r}) \tag{2.13}$$

Fourier form of Poisson's equation and charge density is given by

$$k^2\phi(k) = 4\pi\rho(k) \tag{2.14}$$

and

$$\rho(\mathbf{k}) = \sum_{j=1}^{N} q_j \exp(-i\mathbf{k}\cdot\mathbf{r}_j)\exp(-k^2/4\alpha) \tag{2.15}$$

From the above equations, electrostatic potential is given by

$$\phi(k) = \frac{4\pi}{k^2}\sum_{j=1}^{N} q_j \exp(-i\mathbf{k}\cdot\mathbf{r}_j)\exp(-k^2/4\alpha) \tag{2.16}$$

and

$$\phi(r) = \sum_{\mathbf{k}\neq 0}\sum_{j=1}^{N} \frac{4\pi q_j}{k^2}\exp[i\mathbf{k}\cdot(\mathbf{r}-\mathbf{r}_j)\exp(-k^2/4\alpha) \tag{2.17}$$

Thus, electrostatic potential energy due to compensating charge density is expressed as

$$U_{long-range} = \frac{1}{2}\sum_{i} q_i\phi(r_i) = \frac{1}{2}\sum_{\mathbf{k}\neq 0}\frac{4\pi q_i q_j}{Vk^2}\exp[i\mathbf{k}\cdot(\mathbf{r}_i-\mathbf{r}_j)]\exp(-k^2/4\alpha) \tag{2.18}$$

For efficient convergence, double sum over i and j in the equation above can be simplified into single sum in the following equation [6]:

$$U_{long-range} = \frac{1}{2V}\sum_{\mathbf{k}\neq 0}\frac{4\pi}{k^2}|\rho(\mathbf{k})|^2\exp(-k^2/4\alpha) \tag{2.19}$$

where $\tilde{\rho}(\mathbf{k}) = \sum_{i=1}^{N} q_i exp(i\mathbf{k}\cdot\mathbf{r}_i)$

Above equation includes self interaction between a point charge q_i and Gaussian charge distribution at the same location which needs to be subtracted. Second partial integration

of Poisson's equation gives

$$\phi(r) = \frac{q_i}{r} erf(\sqrt{\alpha} r) \tag{2.20}$$

where $erf(x) = 2\sqrt{\pi} \int_0^x \exp(-a^2) \mathrm{d}a$. Thus, electrostatic potential energy due to self interaction is given by

$$U_{self} = \frac{1}{2} \sum_{i=1}^{N} q_i \phi(r_i) = (\frac{\alpha}{\pi})^{\frac{1}{2}} \sum_{i=1}^{N} q_i^2 \tag{2.21}$$

Lastly, short range potential due to screened point charge, q_i can be calculated. Point charge, q_i, is screened by above Gaussian distribution with net charge $-q_i$. Thus,

$$\phi(r) = \frac{q_i}{r} - \frac{q_i}{r} erf(\sqrt{\alpha} r) \tag{2.22}$$

Thus, electrostatic potential energy due to screened point charge is given by

$$U_{short-range} = \frac{1}{2} \sum_{i \neq j}^{N} q_i q_j erfc(\sqrt{\alpha} r_{ij}) / r_{ij} \tag{2.23}$$

where $erfc(x) = 1 - erf(x)$

The total electrostatic potential is sum of short range potential and long range potential subtracted by self-interaction term:

$$U_{total} = \frac{1}{2} \sum_{i \neq j}^{N} q_i q_j erfc(\sqrt{\alpha} r_{ij}) / r_{ij} + \frac{1}{2V} \sum_{k \neq 0} \frac{4\pi}{k^2} |\rho(\mathbf{k})|^2 \exp(-k^2/4\alpha) - (\frac{\alpha}{\pi})^{\frac{1}{2}} \sum_{i=1}^{N} q_i^2 \tag{2.24}$$

where $\tilde{\rho}(\mathbf{k}) = \sum_{i=1}^{N} q_i exp(i\mathbf{k} \cdot \mathbf{r}_i)$

Particle Mesh Ewald method

Particle Mesh Ewald (PME) method evaluates short range electrostatic potential using cut-off scheme and long range electrostatic interaction potential using fast fourier transform

(FFT). FFT of charge density, $\tilde{\rho}(\mathbf{k})$, requires charge matrix evaluated on a uniform grid by interpolating the point charges. B-spline interpolation function gives higher accuracy than Lagrangian interpolation by increasing the order of interpolation function. Interpolation function of charge density allows to evaluate force analytically by differentiating the electrostatic potential energy.

Ewald summation for reduced periodicity

Some systems such as fluids through infinite channel or membranes require periodicity in only one or two directions. Analogous way to evaluate electrostatic potential in reduced periodicity is to include periodic images only in the direction that periodic boundary condition is applied. However, the double sum over the particles in the Fourier transformation of long range electrostatic interaction is not simplified into a square of a single sum in that case. Thus three-dimensional Ewald summation is computationally cheaper than Ewald summation in reduced periodicity [3]. By using extended box size in the direction that we do not want periodicity, we still can use three dimensional Ewald summation. This method gives distant periodic images and can reduce the effect of periodicity. However, if system a the net dipole moment, electric fields between the periodic images can be generated. The correction term to remove this depolarizing field is developed by Yeh et al. [7]. For infinitely thin slab, the electrostatic energy due to this field is given by

$$U_{correction} = -\frac{2\pi}{V} M_z^2 \tag{2.25}$$

where $M_z = \sum_{i=1}^{N} q_i z_i$. It was found that the above correction term is sufficient if the distance between periodic images in z direction, in which periodicity is removed, is three to five times larger than the box size in x and y direction, in which periodicity is applied. Two dimensional ewald summation (EW2D), three dimensional ewald summation with extended box size (EW3D), and three dimensional ewald summation with correction term (EW3DC)

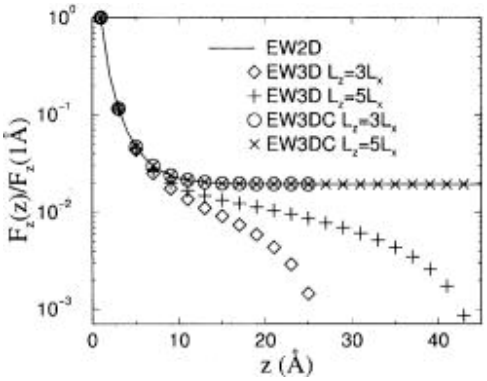

Figure 2.1: Comparison of the z component of the force acting on the unit point charge at (0,0,z) by another oppositely charged unit point charge fixed at (0,0,0) in two-dimensionally periodic systems calculated by different Ewald methods. Two dimensional Ewald summation is denoted by EW2D. Three dimensional Ewald summations without correction term and with correction term are denoted by EW3D and EW3DC, respectively. Periodicity is in x and y direction. L_x and L_z is box size in x direction and z direction, respectively [7].

are compared in figure 2.1. The deviation of three dimensional Ewald summation without correction term is reported by Spohr et al. even with five times larger space applied between periodic images [8].

2.4 Integrating equation of motion

By numerical integration of Newton's equation, molecular trajectories can be found. Several algorithms are developed for integration. Accuracy for large time step is relatively important compared to the speed of algorithm since the time spent on integration is relatively small compared to calculation of intermolecular forces. The accurate algorithm for large time step saves number of steps, that is, number of evaluations of intermolecular forces. Thus, a sophisticated algorithm allowing large time step is advantageous [3]. Leap Frog algorithm, equivalent to Verlet algorithm can be derived from the truncation of Taylor expansion of the atom coordinates. Defining velocities at half-integer time steps, expression for the update of the velocity is given by

$$\mathbf{v}(t + \Delta t/2) = \mathbf{v}(t - \Delta t/2) + \Delta t \mathbf{f}(t)/m \tag{2.26}$$

where $\mathbf{v}$ is velocity, t is time, Δt is time step, and m is mass of atom. Then, expression for the update of the velocity is given by

$$\mathbf{r}(t + \Delta t) = \mathbf{r}(t) + \Delta t \mathbf{v}(t + \Delta t/2) \tag{2.27}$$

where $\mathbf{r}$ is coordinate of atom.

As seen in equations above, the velocity and position of atom are defined at different time. Velocity Verlet algorithm updates positions and velocities at same time as follows:

$$\mathbf{r}(t + \Delta t) = \mathbf{r}(t) + \mathbf{v}(t)\Delta t + \mathbf{f}(t)\Delta t^2/2m \tag{2.28}$$

and

$$\mathbf{v}(t + \Delta t) = \mathbf{v}(t) + (\mathbf{f}(t + \Delta t) + \mathbf{f}(t))\Delta t/2m \tag{2.29}$$

In this scheme, new velocity can be calculated after updating position and force. Velocity Verlet is also equivalent to Verlet algorithm, which is adequate for most MD applications. Other higher-order schemes such as predictor-corrector are also available.

2.5 Temperature coupling

MD simulation samples a microcanonical ensemble (NVE) by integrating Newtonian equations of motion as introduced in the previous section as it keeps energy, number of molecules, volume as constant. Alternative thermodynamic ensembles are available for various purposes by modifying equations of motions. Widely used ensemble is canonical (NVT) in which temperature is constant. In experiment, open system in which temperature is exchanged with

surroundings is often used rather than isolated system. To be compatible with such an experimental system, NVT ensemble can be used. Also, canonical ensemble is popular in studying temperature dependent process, removing heating by external force, or in preventing energy drifts caused by the force truncation and other numerical errors [9].

Various schemes such as Berendsen thermostat, Anderson thermostat, and Nosé-Hoover thermostat are developed for constant temperature in which temperature is defined by

$$T = \frac{2KE}{k_B N_{df}} \tag{2.30}$$

where KE is internal kinetic energy, N_{df} is the number of internal degrees of freedom of the system, and k_B is Boltzmann's constant. Number of internal degree of freedom can be calculated by

$$N_{df} = 3N - N_c - N_r \tag{2.31}$$

where N is number of atoms in the system, N_c is number of constrained degrees of freedom, and N_r=3 under periodic boundary condition. and kinetic energy is obtained by

$$KE = \frac{1}{2}\sum_{i=1}^{N} m_i \mathbf{v}_i^2 \tag{2.32}$$

Berendsen thermostat

In Berendsen thermostat [10], equation of motion is given by

$$\mathbf{a}_i(t) = m_i^{-1} - \frac{1}{2}\tau_B^{-1}[\frac{g}{N_{df}}\frac{T_0}{T(t)} - 1]\mathbf{v}_i(t) \tag{2.33}$$

where τ_B is temperature relaxation time. τ_B can be adjusted for appropriate strength of coupling. However, Berendsen thermostat does not produce canonical ensemble [11]. Only

the limit $\tau_B \to 0$ generates canonical ensemble where Berendsen equation of motion is identical to the Woodcock/Hoover-Evans equation of motion. In the limit $\tau_B \to \infty$, Berendsen thermostat recovers microcanonical ensemble [9].

Nosé-Hoover thermostat

Nosé-Hoover thermostat is based on an extended system by introducing an additional artificial variable with the dimensions of a friction constant proposed by Nosé [12]. The simplified equation of motion, derived by Hoover, is given by

$$\mathbf{a}_i(t) = \mathbf{F}_i m_i^{-1} - \xi \mathbf{v}_i \tag{2.34}$$

where the heat bath parameter, ξ is given by

$$\dot{\xi} = \frac{1}{Q}(T - T_0) \tag{2.35}$$

Mass parameter Q determines the strength of coupling. Nosé-Hoover thermostat samples canonical ensemble. However, temperature controlled by Nosé-Hoover thermostat relaxed through oscillatory fashion, leads to nearly-periodic temperature fluctuation.

2.6 Constraint algorithm

Constraint algorithms are often implemented in integrating equation of motion to maintain optimized geometry of molecules. Various methods based on Lagrangian multiplier to minimize the constraint force are developed. The constraint position of atoms can be written by

$$\mathbf{r}_i(t_0 + \Delta t) = \mathbf{r}_i^0(t_0 + \Delta t) + \frac{1}{2}\frac{(\Delta t)^2}{m_i}\sum \mathbf{g}_{ij}(t_0) \tag{2.36}$$

where $\mathbf{r}_i^0(t_0+\Delta t)$ is position vector at time $t_0+\Delta t$ without constraint and $\mathbf{g}_{ij}(t_0)$ is constraint force. The constraint force is given by

$$\mathbf{g}_{ij}(t_0) = \lambda_{ij}(t_0)\mathbf{r}_{ij}(t_0) \tag{2.37}$$

where λ_{ij} is Lagrangian multiplier. Then, the non linear equation given below can be solved by iteration until reaching an acceptable tolerance.

$$|\mathbf{r}_{ij}|^2 - \mathbf{d}_{ij}^2 = 0 \tag{2.38}$$

SHAKE algorithm [13] solves non linear equation using Gauss-Seidel method. LINCS algorithm [14] approximates the inverse of the Jacobian to a series expansion to reduce computational time. RATTLE algorithm [15] is developed for Velocity-Verlet integration scheme using equation:

$$\mathbf{v}_i(t_0 + \Delta t) = \mathbf{v}_i^0(t_0 + \Delta t) + \frac{1}{2}\frac{\Delta t}{m_i}\sum \mathbf{g}_{ij}(t_0 + \Delta t) \tag{2.39}$$

SETTLE algorithm for rigid water molecules

Many systems involve water molecules as solvent, and efficient algorithm to constraint geometry of water molecules is essential to reduce the total computation time. SETTLE algorithm [16] can be used for water models such as TIP3P and SPC which have triangular geometry. In SETTLE algorithm, the constraint force is not explicitly calculated. Instead, constrained position is analytically determined using Pseudo-Euler angle definition for a canonical triangle. The constrained position of O and two H atoms are obtained based on Cartesian coordinate. The positions of O and two H atoms can be defined as A, B, and C respectively. Positions at time t_0 consists of triangle $\Delta A_0 B_0 C_0$, and at time $t_0 + \Delta t$ without constraint consists of triangle $\Delta A_1 B_1 C_1$. New cartesian coordinate, $X'Y'Z'$, centered at

center of mass of triangle $\Delta A_1B_1C_1$ can be defined. $X'Y'$ plane is parallel to plane contains $\Delta A_0B_0C_0$ and $Y'Z'$ plane includes A_1. Constraint force applies on bonded atoms with same magnitude but with opposite direction, the sum of constraint forces is zero. Thus, center of mass of $\Delta A_1B_1C_1$ and $\Delta A_3B_3C_3$, the triangle after applying constraint, are coincident. We can place $\Delta A_0B_0C_0$ on the $X'Y'$ plane and let center of mass of $\Delta A_0B_0C_0$ be on the origin of $X'Y'Z'$. Then, constraint geometry of water molecules can be determined after the rotation of $\Delta A_0B_0C_0$ around origins. Rotations around Y', X',and Z' axis can be performed by angles ψ, ϕ, and θ, respectively. The triangles after each rotations indicate $\Delta a_1b_1c_1$, $\Delta a_2b_2b_2$, and $\Delta a_3b_3c_3$, respectively. Then, ψ, ϕ, and θ, and final coordinates of $\Delta A_3B_3C_3(= \Delta a_3b_3c_3)$ can be determined analytically.

The coordinates of point A in $X'Y'Z'$ can be denoted by $A = (X'_A, Y'_A, Z'_A)$ or $A' = (s, t, u)$. The coordinates of $\Delta a_0b_0c_0$ in $X'Y'Z'$ can be expressed by

$$a'_0 = (0, r_a, 0) \tag{2.40}$$

$$b'_0 = (-r_c, -r_b, 0) \tag{2.41}$$

$$c'_0 = (r_c, -r_b, 0) \tag{2.42}$$

Then, $\Delta a_1b_1c_1$ obtained by the rotation ψ of $\Delta a_0b_0c_0$ around Y' axis is given by

$$a'_1 = (0, r_a, 0) \tag{2.43}$$

$$b'_1 = (-r_c \cos\psi, -r_b, r_c \sin\psi) \tag{2.44}$$

$$c'_1 = (r_c \cos\psi, -r_b, -r_c \sin\psi) \tag{2.45}$$

and $\Delta a_2b_2c_2$ obtained by the rotation ϕ of $\Delta a_1b_1c_1$ around X' axis is

$$a'_2 = (0, r_c \cos\phi, r_c \sin\phi) \tag{2.46}$$

$$b_2' = (-r_c \cos\psi, -r_b \cos\phi - r_c \sin\psi \sin\phi, -r_b \sin\phi + r_c \sin\psi \cos\phi) \tag{2.47}$$

$$c_2' = (r_c \cos\psi, -r_b \cos\phi + r_c \sin\psi \sin\phi, -r_b \sin\phi - r_c \sin\psi \cos\phi) \tag{2.48}$$

Finally, $\Delta a_3 b_3 c_3$ by the rotation θ around Z' axis can be expressed by

$$a_3' = (-r_c \cos\phi \cos\theta, r_c \cos\phi \cos\theta, r_c \sin\phi) \tag{2.49}$$

$b_3' = (-r_c \cos\phi \cos\theta + r_b \cos\phi \sin\theta + r_c \sin\psi \sin\phi \sin\theta,$

$$-r_c \cos\psi \sin\theta - r_b \cos\phi \cos\theta - r_c \sin\psi \sin\phi \cos\theta, -r_b \sin\phi + r_c \sin\psi \cos\phi) \tag{2.50}$$

$c_3' = (r_c cos\psi \cos\theta + r_b cos\phi \sin\theta - r_c \sin\psi \sin\phi \sin\theta,$

$$r_c \cos\psi \sin\theta - r_b \cos\phi \cos\theta + r_c \sin\psi \cos\theta, -r_b \sin\phi - r_c \sin\psi \cos\phi) \tag{2.51}$$

Z' coordinates of $\Delta a_2 b_2 c_2$ and $\Delta a_3 b_3 c_3$ are equal to each other since $\Delta a_3 b_3 c_3$ are rotated around Z' axis. Also, Z' coordinates of $\Delta a_3 b_3 c_3$ and $\Delta A_1 B_1 C_1$ are identical since the constraint forces acting at time t_0 along the bonds of $\Delta A_0 B_0 C_0$ are on the $X'Y'$ plane. Hence, Z' coordinates of $\Delta A_1 B_1 C_1$ and $\Delta a_2 b_2 c_2$ are indentical:

$$Z'_{A1} = r_a \sin\phi \tag{2.52}$$

$$Z'_{B1} = -r_b \sin\phi + r_c \sin\psi \cos\phi \tag{2.53}$$

$$Z'_{C1} = -r_b \sin\phi - r_c \sin\psi \cos\phi \tag{2.54}$$

Then, angle ϕ and ψ can be calculated through equations

$$\sin\phi = Z'_{A1}/r_a \tag{2.55}$$

and

$$\sin\psi = \frac{Z'_{B1} - Z'_{C1}}{2r_c \cos\phi} \tag{2.56}$$

Finally, θ can be calculated using the condition that constraint forces acting along the bond have same magnitudes and opposite direction.

$$\sin\theta = \frac{\alpha\gamma - \beta\sqrt{\alpha^2 + \beta^2 - \gamma^2}}{\alpha^2 + \beta^2} \tag{2.57}$$

where

$$\alpha = (X'_{B_0} - X'_{C_0})X'_{b_2} + (Y'_{B_0} - Y'_{A_0})Y'_{b_2} + (Y'_{C_0} - Y'_{A_0})Y'_{c_2} \tag{2.58}$$

$$\beta = (Y'_{C_0} - Y'_{B_0})X'_{b_2} + (X'_{B_0} - X'_{A_0})Y'_{b_2} + (X'_{C_0} - X'_{A_0})Y'_{c_2} \tag{2.59}$$

$$\gamma = (X'_{B_0} - X'_{A_0})Y'_{B_1} - (Y'_{B_0} - Y'_{A_0})X'_{B_1} + (X'_{C_0} - X'_{A_0})Y'_{C_1} - (Y'_{C_0} - Y'_{A_0})X'_{C_1} \tag{2.60}$$

It is reported that SETTLE algorithms is seven times faster than RATTLE with the tolerance of 5×10^{-4} and 1×10^{-4} Å, which are commonly used in constraint algorithm, using scalar machines. On a vector machine, SETTLE is 39 times faster than RATTLE with the tolerance of 1×10^{-4} Å due to the noniterative nature of SETTLE algorithm.

2.7 Molecular models for water

Various molecular models for water have been developed to be in agreement with a certain set of physical structures or parameters such as radial distribution function, the density anomaly, or other critical parameters [17]. How successfully the water models predict basic properties of bulk water determines the reliability of water models [18]. Table 2.2 compares physical properties obtained from the experiment and simulations using various water models.

Various water models have different potential functions, potential parameters, and inter-

Table 2.2: Physical properties of liquid water at 25 C° and 1 atm calculated from MD simulations using different water models and the experiment [17]. † is calculated at 10 C°. μ_{dip}, ϵ, D_{self} and Energy denote the dipole moment, dielectric constant, self diffusion coefficient, and average configurational energy, respectively

Model	μ_{dip} (Debye)	ϵ	$D_{self}(10^{-5}\mathrm{cm}^2/\mathrm{s})$	Energy (kJ/mol)
SSD	2.35	72	2.13	-40.2
SPC	2.27	65	3.85	-41.0
SPC/E	2.35	71	2.49	-41.5
TIP3P	2.35	82	5.19	-41.1
TIP4P	2.28	$53^{\dagger}$	3.29	-41.8
TIP5P	2.29	81.5	2.62	-41.3
Expt.	2.65	78.4	2.30	-41.5

acting sites on which potential is applied. Potentials for water models such as simple point charge (SPC) [19] and TIPnP [20, 21, 22] are represented by LJ potential and electrostatic potential. On the other hand, soft sticky dipole (SSD) [23] model is represented by Lennard-Jones potential, point dipole-point dipole potential, and tetrahedral sticky potential. Water models such as SPC, SPC/E [24], and TIP3P use three interacting sites while ST2 [25] or TIP5P use five interacting sites. Fixed charges and sites for coulomb interaction can not capture the polarizability of water molecules. Shell water (SW) [26] model, flexible as well as rigid, has been developed to include the polarizability of water molecules. Electronic degrees of freedom was included by dummy atoms on the bisector of the water molecules connected by harmonic spring. Polarizable point charge (PPC) [27] model also can be used to include polarization response of water molecules to a local electric field if explicit calculation of electric field is available. However polarizable water model requires additional computation cost.

Widely used water model is extended simple point charge (SPC/E) model improved from SPC model. SPC/E water model gives reasonably accurate diffusion coefficient and dielectric constant. Three interacting sites of SPC/E water model corresponds to O and two H atoms as shown in figure 2.2. The bond length of O-H is 0.16 nm and The bond angle of O-H-O is 109.47°. Charges of O and H are 0.4238 e and -0.8476 e, respectively. LJ interaction is

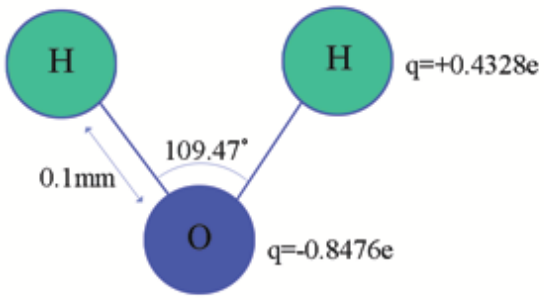

Figure 2.2: Geometry of SPC/E water model

applied on O with parameters $\sigma = 0.3169$ nm and $\epsilon = 0.6502$ kJ/mol.

2.8 Reverse osmosis simulation

Simulation set-up

Schematics and snap shots of simulation set-up are described in Fig. 2.3(a) and Fig. 2.3(b), respectively. The system consisted of a membrane, solution chamber, pure water chamber and pressure piston. The solution chamber contained water and 4M KCl. A simple point charge-extended (SPC/E) model was used for water and ions were modeled as charged LJ atoms [28]. The pure water chamber contained only water molecules. Pressure pistons were made of silicon atoms with a GROMOS96 force-field. By applying external forces on pressure pistons, the z location of pressure pistons are independently self-adjusted to maintain the desired pressure [29].To prevent the distortion of the pressure pistons, the average force between the piston atoms and the liquid atoms are added to the external force, $f_z = (\sum_{i=1}^{M} \sum_{j=1}^{N} f_{zij} + AP_{ext})/M$, applied to each piston atom at every time step, where M and N are the number of molecules in pressure piston and in liquid, respectively; f_{zij} is the z component force acting on ith pressure piston molecule due to jth liquid molecule; A is

the cross-sectional area of chambers and P_{ext} is the external pressure. Periodicity is applied in the x- and y-direction.

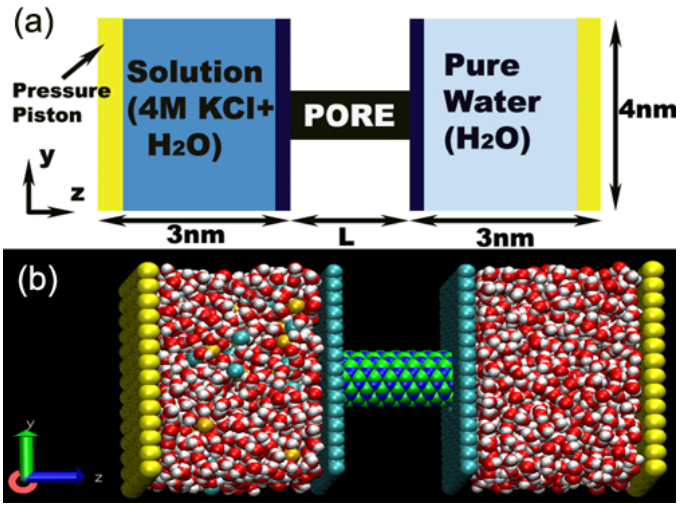

Figure 2.3: (a)Schematics and (b)Snap-shot of simulation set up

Simulation Method

MD simulations were performed using modified GROMACS 3.3.1 [30]. A Nosé-Hoover thermostat with a time constant of 0.1 ps was employed to maintain the temperature of the fluid at 300K. Electrostatic interaction was calculated using the particle mesh Ewald (PME) method [31] with a 0.1 nm real-space cutoff, 1.5 Å reciprocal space gridding, and splines of order 4 with a 10^{-5} tolerance [31]. 1 nm cutoff distance was used in calculating LJ interaction. The SETTLE algorithm was used to constrain the geometry of water molecules. The equations of motion were integrated by using a leapfrog algorithm. Simulation time step was 1.0 fs and trajectories were sampled every 1.0 ps for analysis. Each chamber was equilibrated for 2.0 ns by blocking the pore, and external pressure was applied for 1.0 ns before opening the pore to prevent initial osmosis. A pressure piston attached to the pure water chamber was maintained at 100 MPa, and different pressures ranging from 100 MPa to 600 MPa were applied to the pressure piston attached to the solution chamber. After removing the blocks of pore, water molecules moved from the solution chamber to the pure

water chamber against the osmotic pressure gradient while the ions did not go through. Simulation was run until at least 180 water molecules were transported to the pure water chamber.

Chapter 3

Enhanced reverse osmosis using nanotube membranes

3.1 Introduction

Reverse-osmosis (RO) is a widely used membrane separation technology proven to be a good barrier for inorganic ions, and biomolecules including amino acids, and emerging organic pollutants such as disinfection byproducts (DBPs) and endocrine-disrupting chemicals (EDCs) [32]. The performance of the membrane is determined by the water flux and salt rejection rate; that is, high water flux and salt rejection rate are crucial for an efficient RO process. The water flux and salt rejection rate for commercially used cellulose acetate RO membranes are 3.93×10^{-9} m/s/kPa and 98 %, respectively [32]. Considering that biological cell membrane composed of aquaporin 1 (AQP1) water channels, abundant in kidneys, show the considerably higher water flux of 3.715×10^{-7} m/s/kPa and perfect ion rejection rates of 100 % [33], nano-enabled technology mimicking biological systems can achieve more effective membrane separation process.

Single-walled carbon nanotubes (SWCNTs) have been intensively studied due to their interesting mechanical, chemical, thermal, and electronic properties, and applied in various fields such as sensors [34], nanofluidics [35], energy storage [36], field-emission [37], etc. After Hummer et al. [38] studied water conduction through subnanometer size pores of (6,6) SWCNT using molecular dynamics, the application of carbon nanotubes (CNTs) in biological systems has been discussed in conjunction with fast osmotic water flux [39].

The study of the chirality effect of CNT showed that the water configuration inside (10,0) polarizable CNT is similar to a AQP1 water channel [40]. Inside AQP 1 and (10,0) CNT, wa-

ter dipole vectors point towards the water reservoir, resulting in the formation of an L defect in the center region, preventing proton conduction. In (6,6) CNT, dipole vectors of all water molecules point towards either the top or the bottom reservoir, and the diffusion coefficient was higher compared to (10,0) CNT. Recently fabricated sub 2-nm CNT membranes [41] proved the potential of CNT membranes in water filtration applications by observing several orders of magnitude higher water flux compared to continuum hydrodynamics.

In this chapter, the RO performance of CNT are compared to boron nitride nanotube (BNNT) and polymethyl methacrylate (PMMA) using molecular dynamics simulations. BNNT is another class of nanotube, which can replace CNT in various applications requiring chemical stability and electrical insulation. However, currently there are only limited number of studies on water transport behavior [42]. PMMA is class of polymer widely used due to its optical and bio-compatible properties.

Molecular dynamics (MD) simulation has proven useful in observing nano-scale dynamics of fluids as well as solids, and has successfully simulated various flows such as Poiseuille flow [43], Couette flow [44], osmosis [39, 45], electro-osmosis [46], etc. Murad et al. performed reverse-osmosis simulations through artificial pore and zeolite membrane [47, 48]. However quantification of water flux had difficulty since RO has been observed in transient state from non-equilibrium to equilibrium. For quantitative comparison of three different membrane types, non-equilibrium and steady-state RO simulation was performed by introducing pressure pistons.

The simulation results indicated that the water flux through BNNT and CNT are significantly higher compared to PMMA, and slightly higher through BNNT compared to CNT, i.e., $J_{BNNT} \gtrapprox J_{CNT} > J_{PMMA}$. This result was contradictory to the solution-diffusion model widely used in RO. Also, water flux was several orders of magnitude higher than the pore model. A theoretical single-file "hopping" model was consistent with the simulation results. The correlation between entrance time and translocation time in collective water transport was discussed. Using PMF analysis, the irregular pore surface character of PMMA is found

to be the factor in low water flux. The higher water flux through BNNT was explained by stronger Van der Waals interaction between BNNT and water.

3.2 Membrane preparation: BNNT, CNT, and PMMA

We prepared three membrane types: BNNT, CNT, and PMMA. For BNNT and CNT, we considered open-ended single-walled nanotubes (SWNTs) with (6,6) configuration. The initial C-C and B-N bond length were 1.42 Å and 1.44 Å, respectively. The buckled BNNT were formed by moving nitride atoms slightly outwards (by 0.032 Å) and boron atoms slightly inwards (by 0.032 Å) from the tube center. This buckled BNNT geometry was consistent with previous *ab initio* calculations [49]. The membrane wall for BNNT and CNT consisted of hydrophobic pseudoatoms [40] to be consistent with the hydrophobicity of BNNT, CNT, and PMMA.

To make comparable pore size and membrane thickness to BNNT and CNT, we positioned isotactic PMMA chains on the outside of (3,3) CNT. Then, density was adjusted to an experimental value of 1.18 g/cc at 300 K by reducing the simulation box size. Configuration was equilibrated for 5 ns, and temperature annealing cycles involving NVT dynamics for 5 ns at 700K was repeated three times to prevent the system from getting trapped in a local minimum energy state. To reduce the pore diameter further, the CNT was replaced to a one dimensional carbon chain, and equilibrated again. After removing the carbon chain, PMMA was relaxed for 100 ps.

The obtained lengths of BNNT, CNT, and PMMA pores were 2.135 nm, 2.090 nm and 1.8 nm, respectively. Diameters for the BNNT and CNT were 0.83 nm and 0.81 nm, respectively, while the PMMA pore had a minimum diameter of 0.82 nm and an average diameter of 1.08 nm. The diameter of the pore along the pore axes are plotted in Fig. 3.1(a). Note that CNT and BNNT have uniform pore diameter while PMMA has irregular pore diameter

due to a tangled polymer chain. The charge distribution of the PMMA pore surface are plotted in Fig. 3.1(b). (6,6) CNT and BNNT was considered to be non-polar [38, 42]. A GROMACS force-field was used for PMMA. Lennard-Jones (LJ) parameters for BNNT and CNT were taken from [50] and [51], respectively.

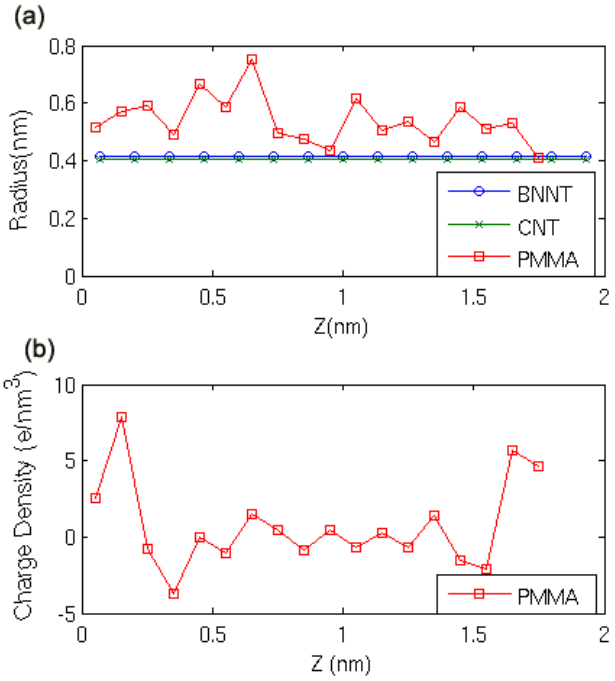

Figure 3.1: (a) pore radius and (b) pore charge distribution for BNNT, CNT, and PMMA pore. BNNT and CNT are assumed to be non-polar. BNNT and CNT have the uniform pore radius while PMMA has irregular pore radius and charge distribution

3.3 Results and analysis

Water flux and comparison of RO membrane

The pressure difference between solution chamber and pure water chamber was measured from the forces exerted on membrane walls connected with the BNNT [45]. The pressure differences were maintained at the desired values.The number of water molecules accumulated in the pure water chamber and the decrease in the number of water molecules in the

solution chamber with time are plotted in Fig. 3.2. With the constant pressure difference, steady-state water flux by reverse-osmosis is observed since the change of the net thermal driving force due to the increase in osmotic potential with time is negligible.

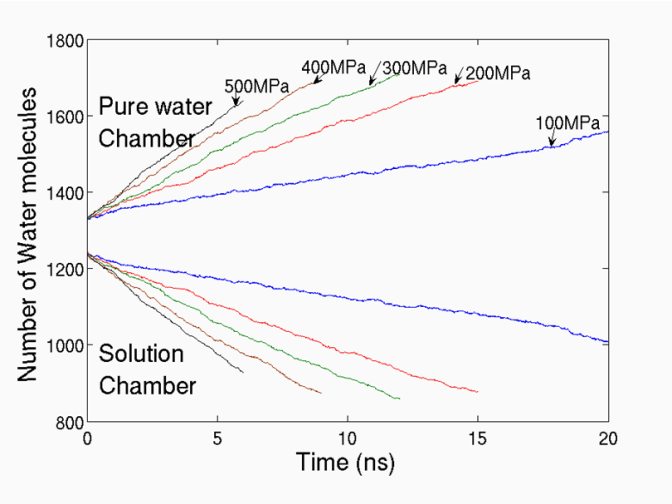

Figure 3.2: Variation of water occupancy in the pure water chamber and solution chamber with time for BNNT pore. Each line is for a different ΔP, pressure drops of 100 MPa, 200 MPa, 300 MPa, 400 MPa and 500 MPa were considered.

Simulations were repeated with BNNT, CNT, and PMMA membranes. Water flux for each ΔP was calculated by dividing total number of water molecules transported from the solution chamber to the pure water chamber by total simulation time. Water flux varied linearly with applied ΔP as expected at near-equilibrium condition. It was reported that near-equilibrium condition does not necessarily require the small pressure gradient [52]. We observed a higher water flux for BNNT and CNT membranes compared to the PMMA membrane (see Fig. 3.3). Also, the water flux for the BNNT membrane was slightly higher compared to the CNT membrane.

Permeation coefficient of membranes

The mathematical description of permeation in all membranes can be expressed as Eq. 3.1 when the process is not far from equilibrium and water flux is linearly varied with chemical potential gradient:

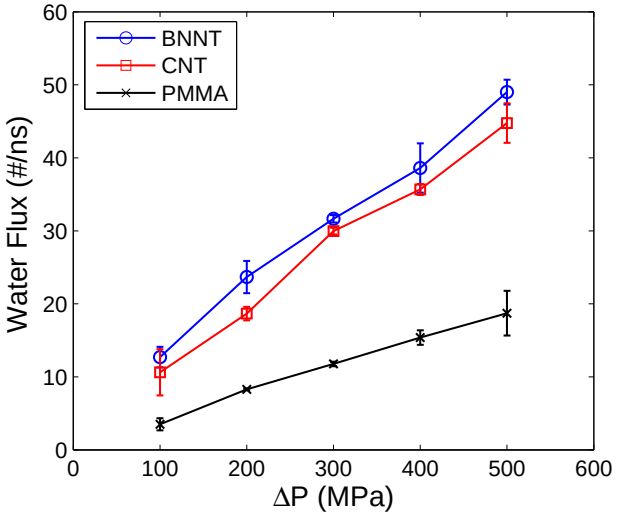

Figure 3.3: Variation of the RO water flux with applied pressure gradient for BNNT, CNT, and PMMA pores. Water flux for BNNT and CNT are considerably higher compared to PMMA, and water flux for BNNT are slightly higher compared to CNT.

$$J_n = p_n \frac{\Delta\mu}{k_B T} \tag{3.1}$$

where J_n (water molecules/ns) is water flux, p_n (water molecules/ns) is the permeation coefficient, and $\Delta\mu$ is chemical potential gradient, k_B is Boltzmann constant, and T is temperature. This simple expression is extremely useful because many processes involve different driving forces (pressure, concentration, temperature, electro-motive forces, etc.), and overall driving force producing movement of permeant is the chemical potential gradient [53]. In the RO process, involving driving force is pressure gradient and concentration gradient. For incompressible liquid and dilute solutions, chemical potential gradient in the RO process follows Eq. 3.2 [54]:

$$\frac{\Delta\mu}{k_B T} = -V_w \Delta C_s + \frac{V_w}{N_A k_B T} \Delta P \tag{3.2}$$

where V_w (cm^3/mol) is molar volume, C_s (mol/cm^3) is salt concentration, N_A is the Avogadro number, and ΔP (MPa) is pressure gradient.

Applied pressure gradient (100 MPa∼500 MPa) and concentration gradient (∼8 M) were used to determine chemical potential gradient by Eq. 3.2, and permeation coefficient, p_n, was determined by linear regression of J_n vs. $\Delta\mu/k_BT$. Calculated values were 14.7 water molecules/ns, 13.4 water molecules/ns and 5.6 water molecules/ns for BNNT, CNT and PMMA respectively. Consequently BNNT and CNT membrane had an order of magnitude higher permeation coefficients compared to PMMA membrane. The measured permeation coefficient of PMMA membrane is higher than the experimentally measured value for PMMA membranes in the nano filtration (NF) range requiring a larger pore size than RO. However, it is noteworthy that permeation coefficient of PMMA is comparable to the experimentally measured the permeation coefficient of aquaporin 1 water channel (∼3.0 water molecules/ns) [33], considering that both PMMA and biological channels share similar structural properties (i.e., irregular pore surface and inhomogeneous charge distribution) since PMMA considered in this study also has well defined pore. The diameter of the aquaporin 1 water channel is similar to our membranes and water molecules are transported in single-file manner, as will be discussed later.

Theoretical model: solution-diffusion model and pore model

Solution-diffusion model [55] and pore model [56] are two general theoretical models used to predict the water flux in RO. The solution-diffusion model assumes both the solute and solvent individually diffuse through the membrane due to their uncoupled, own chemical potential gradients. Since the water flux is only by diffusion, Fick's law and Henry's law are used to derive the water flux, given by

$$J_w = \frac{D_{wm}C_{wm}}{RT}\frac{\Delta\mu_w}{L} \tag{3.3}$$

where J_w is water flux, D_{wm} is the diffusion coefficient, C_{wm} is water concentration in the membrane, R is the gas constant, T is temperature, L is membrane length, and $\Delta\mu$ is

chemical potential gradient defined by Eq. 3.2.

Pore model assumes the transport of water takes place by viscous flow through uniform membrane pores and transport of solute occurs by diffusion and convection in these pores. When solutes are impermeable to membrane, from Poiseuille's law, water flux is given by

$$J_w = \frac{\epsilon R^2 \Delta P}{8\eta\tau Ł} \tag{3.4}$$

where J_w is water flux, ϵ is the porosity of the membrane, R is pore radius, η is the viscosity of water, τ is tortuosity, and L is membrane length.

To compare the theoretical models to our simulation results, D_{wm} and C_{wm} are determined from the equilibrium simulation. The axial diffusion coefficient, D_{wm}, is related to the slope of the mean-squared displacement (MSD) by the well-known Einstein relation:

$$D_{wm} = \frac{1}{2} \lim_{t\to\infty} \frac{< |r(t) - r(0)|^2 >}{\Delta t} \tag{3.5}$$

where $r(t)$ is the position vector at time t.

Each theoretical model is plotted in Fig. 3.4 with simulation results. With the solution-diffusion model, higher water flux through BNNT and CNT is not explained. The higher concentration inside PMMA resulted in the higher water flux through PMMA compared to BNNT and CNT, which is contradictory to our simulation results. Simulation results had $3 \sim 4$ orders of magnitude higher water flux compared to the pore model. It is obvious that Poiseuille's flow, which excellently modeled continuum flow, failed to describe RO when pore diameter is comparable to the diameter of the water molecules. Also, the pore model did not take into account the effect of membrane property on water flux.

Single-file water transport

The failure of the solution-diffusion model and pore model can be explained by different transport mechanism through these membranes, called single-file "hopping" transport. When pore diameter is comparable to the diameter of water molecules, water molecules can

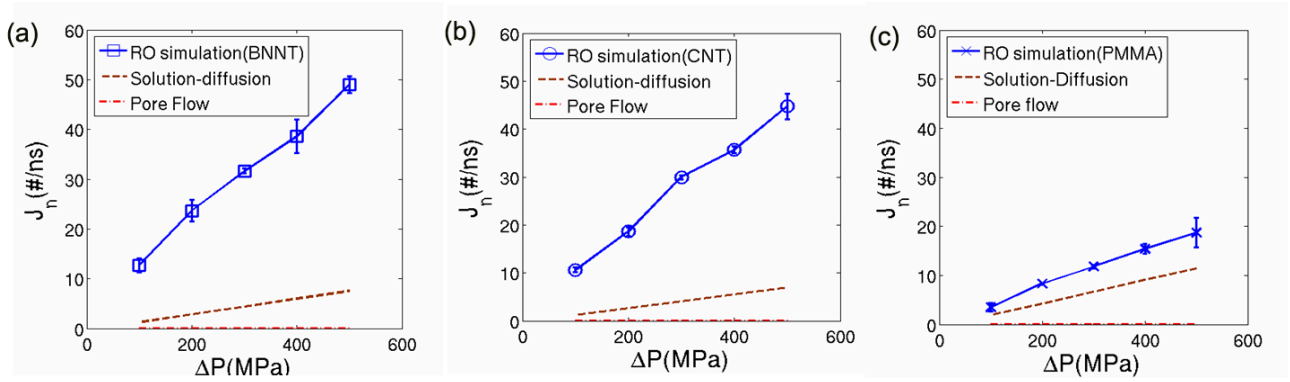

Figure 3.4: Comparison of simulation results for (a) BNNT, (b) CNT, and (c) PMMA to theoretical models: solution-diffusion model and pore model. Water flux of simulation results are three to four orders of magnitude higher compared to pore model. Solution-diffusion model also fails to explain enhanced water flux for BNNT and CNT.

not "overtake" the other water molecules and they are transported in single-file manner. The motion of water molecules formed single-file are highly correlated, requiring the concomitant motion of all molecules. The trajectories of all water molecules inside pores clearly show this tendency (see Fig. 3.5). As shown in Fig. 3.5, the collective motion of all water molecules inside BNNT and CNT was observed (CNT is not shown here due to the similarity to BNNT). In the case of PMMA, more than single-file water molecules are occupied at the pore mouth region and the formed single-files are often broken due to the irregular pore diameter.

The transport of single-file water molecules can be explained by a hopping mechanism as described in Fig. 3.6. The single-file water molecules hop about a water-water distance, d, after an average waiting time of τ. The hopping rate, k, defined as the number of hopping events during the unit time, is given by $k = 1/\tau$. The net water flux is the difference between forward hopping rate, k^+, and the backward hopping rate, k^-. In equilibrium, $k^+ = k^- = k^0$, thus $k_0 = (1/2)k$.

Using reaction rate theory, the water flux and chemical potential gradient is related

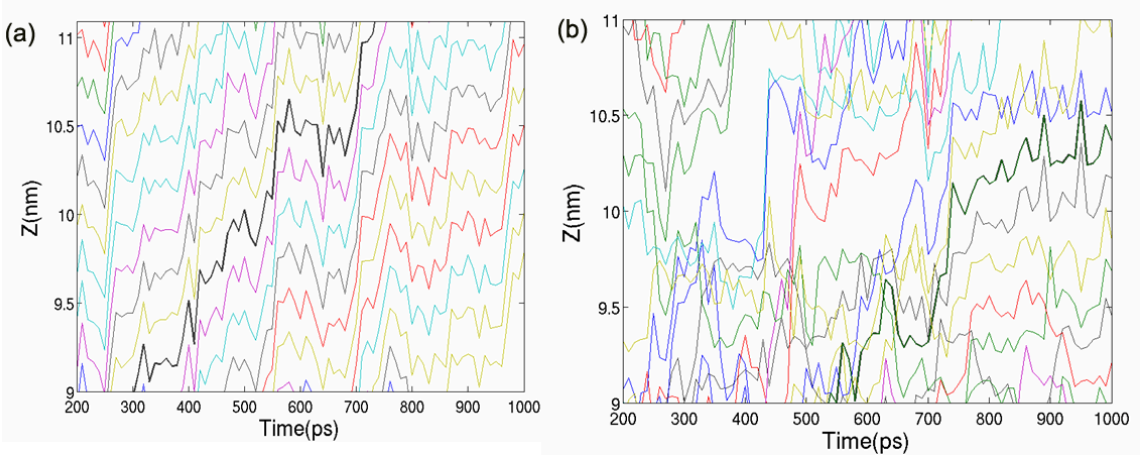

Figure 3.5: Trajectory of water molecules inside (a) BNNT and (b) PMMA pore. Water molecules formed single-file and transported by concerted motion. Inside PMMA, single-file water molecules are partially formed.

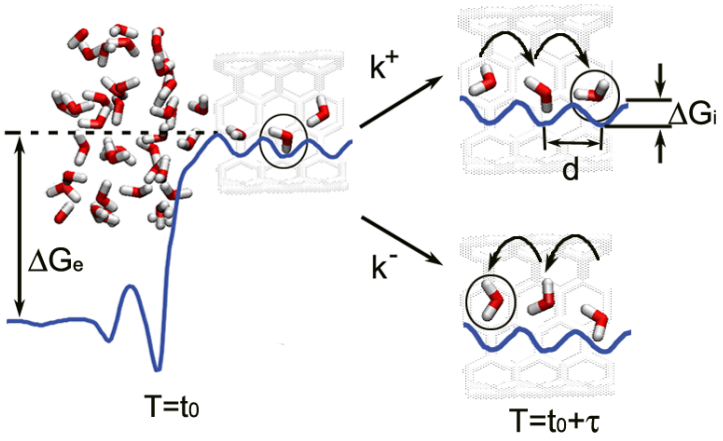

Figure 3.6: Water configuration snap shot and the underlying PMF profile for CNT pore. ΔG_e and ΔG_i denote energy barrier at pore entrance and inside, respectively. Water molecules hop to the next PMF minima in a time interval, τ. Bidirectional hopping rate, $k\,(\mathrm{ns}^{-1})$ is defined by number of hops during unit time. $k = k^+ + k^-$ where k^+ is the forward hopping rate (shown in top right) and k^- is the backward hopping rate (shown in bottom right). At equilibrium, $k^+ = k^- = k_0$

by [52, 57],

$$J_n = k_0 \frac{\Delta\mu}{k_B T} \tag{3.6}$$

k_0 is obtained from equilibrium simulations. k_0 is determined by counting all the forward and backward hopping events during the simulation time. The movement of water molecules from one minimum of PMF to the next minimum of PMF was counted as one hopping event. For PMMA, the hopping rate is obtained in the portion of the pore where single-file water is observed. The values of k_0 computed from the equilibrium simulations are k_0=16.0 ns^{-1}, 15.0 ns^{-1} and 3.0 ns^{-1} for the BNNT, CNT and PMMA membranes, respectively. The comparison to simulation results are plotted in Fig. 3.7. Even though PMMA has error due to the intermittency and vacancy of single-file, BNNT and CNT are in good agreement with the theoretical expression. Also, this single-file transport model successfully predicted $J_{BNNT} \gtrsim J_{CNT} > J_{PMMA}$.

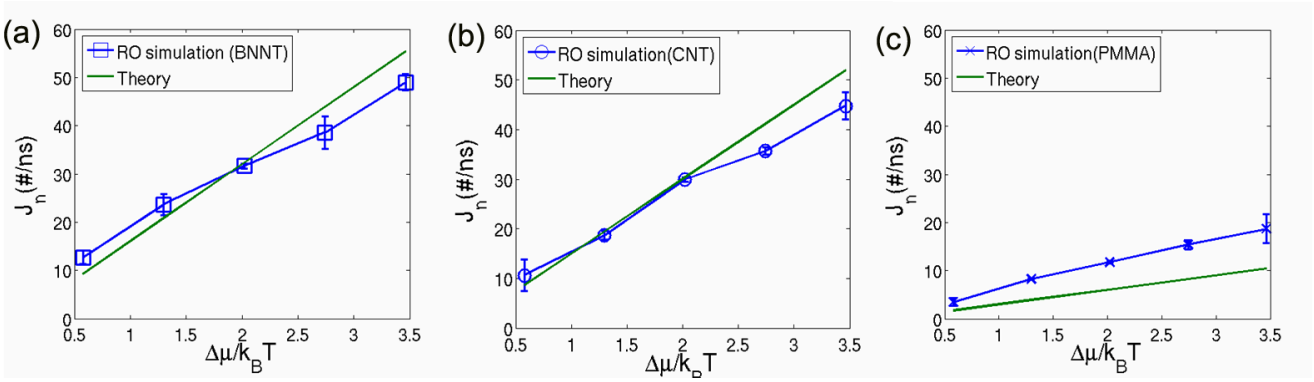

Figure 3.7: Comparison of simulation results for (a) BNNT, (b) CNT, and (c) PMMA to theoretical single file models. The difference for PMMA can be explained by the single-file intermittency and vacancy (see Fig. 3.5) inside PMMA pore. BNNT and CNT are in good agreement with the theoretical model.

Potential of mean force analysis

We showed the permeation coefficient, p_n, was in reasonable agreement with the equilibrium hopping rate, k_0, in the previous section. We performed potential of mean force (PMF) analysis to achieve a better understanding of the determinants affecting k_0, to understand

the determinants affecting fast RO. The free energy profile along the water passage can be obtained by integration of the average forces acting on the water molecule, i.e.:

$$PMF = \int_{z_0}^{z} < F_i(Z') > dz' \tag{3.7}$$

where z_0 is the reference position where the average force vanishes. We decomposed the PMF of water into contributions arising from different types of interactions such as water-water interaction, water-membrane LJ interaction, and water-membrane electrostatic interaction.

Fig. 3.8(a) and (b) show water-water and water-membrane PMFs for BNNT and CNT, respectively. The larger hopping rate for BNNT than that for CNT can be explained from the lower energy barrier present at the pore entrance and in the pore interior. The energy barrier at the pore entrance for BNNT and CNT membranes is $5.15\,k_BT$ and $5.273\,k_BT$ and the average energy barrier in the pore interior is $0.23\,k_BT$ and $0.47\,k_BT$ respectively. It appears that series of energy barrier inside pore is mainly due to the water-water interaction. It has been discussed that collective motion of single-file water molecules, i.e., the correlation between water positions inside the pore develops the interior energy barrier [58]. The main access energy barrier to the pore is developed by losing on average two out of four hydrogen bonds, and the lost energy is partially compensated by water-membrane interaction [38]. Therefore stronger Van der Waals interaction between BNNT and water (ϵ_{B-O}=0.5082 kJ/mol ,ϵ_{N-O}=0.6277 kJ/mol) compared to CNT and water (ϵ_{C-O}=0.4340 kJ/mol) is the primary reason for higher water permeability as it lowers the PMF at the pore entrance.

Fig. 3.9 shows the PMF components for PMMA. Unlike BNNT and CNT pores, in which water molecules form a single-file water chain, in the PMMA pore, more than single-file water is present near the pore mouth and water density decreases as we approach the interior of the pore. Even though the energy barrier at the pore entrance ($4.35\,k_BT$) is lower compared to the BNNT and CNT pores, the average energy barrier inside the pore is higher

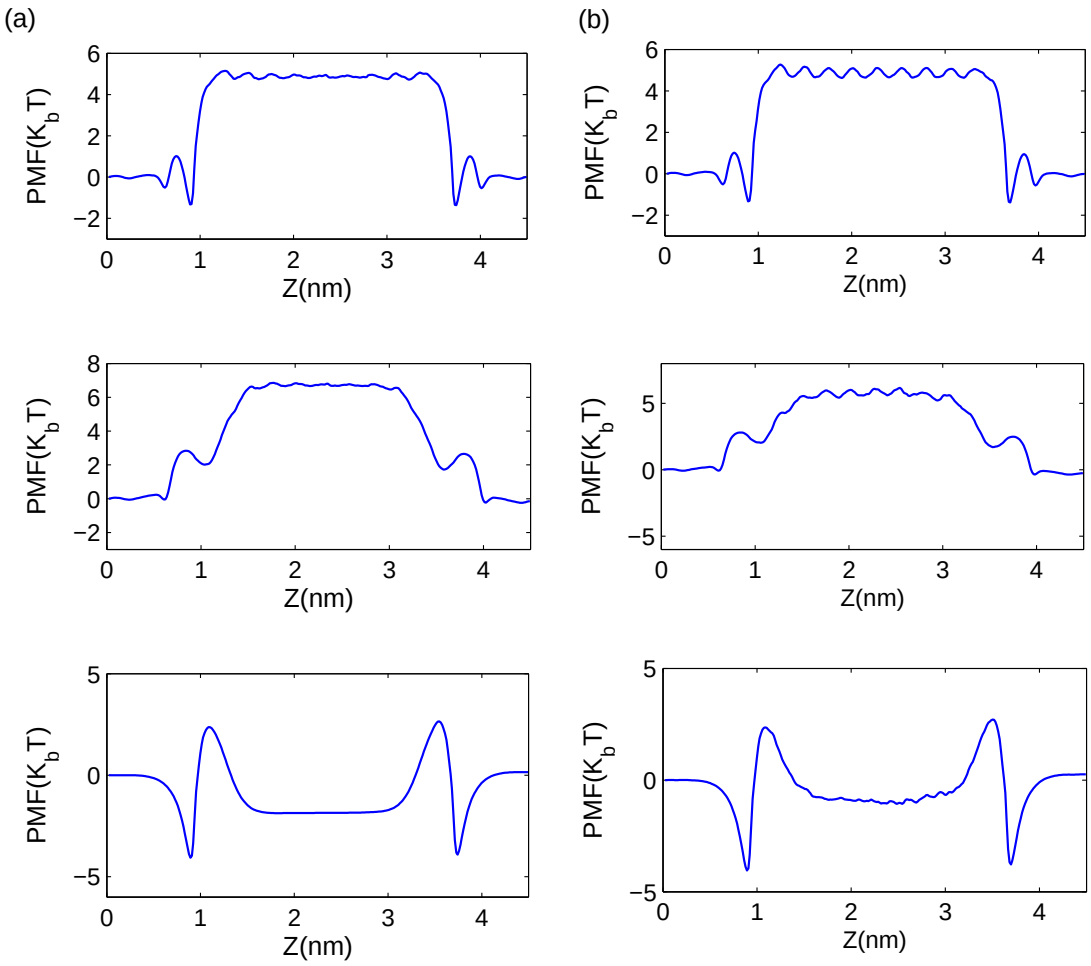

Figure 3.8: PMF decomposition for (a) BNNT and (b) CNT. Top, center and bottom figures are total PMF, water-water interaction PMF, water-membrane interaction PMF, respectively. Energy barriers at pore entrance for BNNT and CNT are 5.15 k_BT and 5.273 k_BT, respectively.

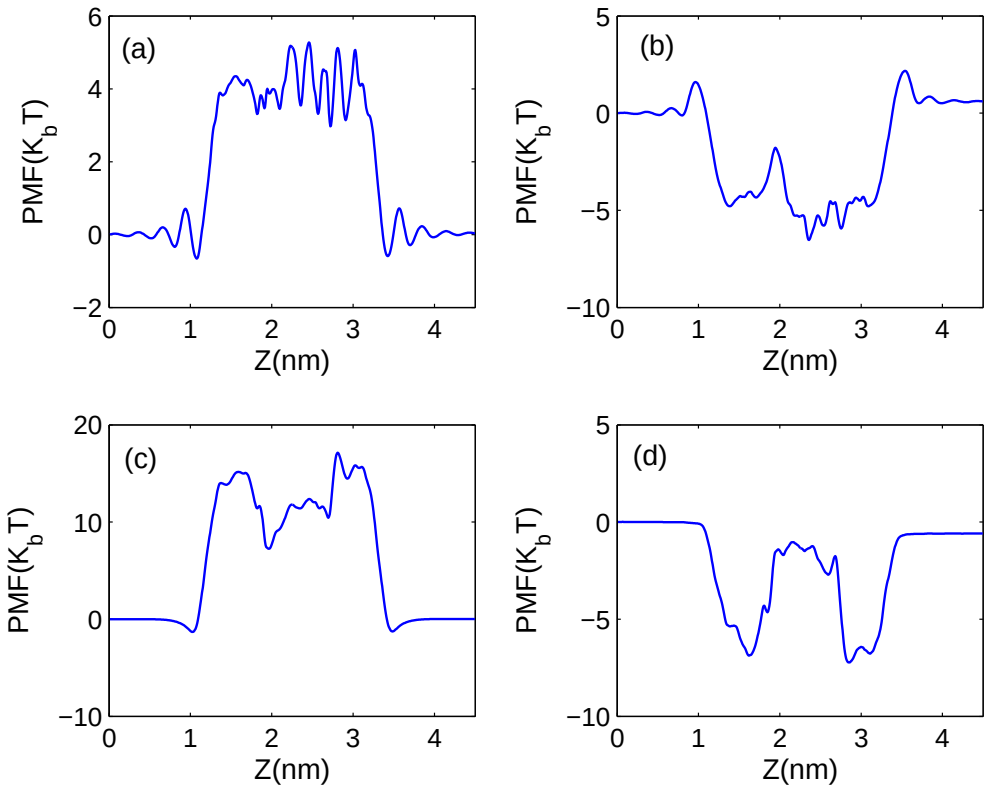

Figure 3.9: PMF components for PMMA. (a) Total PMF (b) water-water interaction (c) water-membrane LJ inetaction (d) water-membrane electrostatics interaction.

($1.76\,k_BT$). Irregular PMMA pore structure and inhomogeneous charge distribution contribute to the high energy barrier present in the pore interior, leading to the observed low flux. Note that PMF profile due to the water-membrane LJ and electrostatic interaction is irregular for PMMA while they are flat for BNNT and CNT.

Entrance and translocation time

To further understand the transport behavior of single-file RO, using the MD simulation data we studied the correlation between the entrance time and the translocation time. Entrance time (denoted by T_e) was calculated by averaging successive entrance events of water molecules that have successfully translocated, and translocation time (denoted by T_t) was measured by averaging the time interval between entrance and exit events of the water molecules that have completely translocated. Variation of the entrance and translocation times with the pressure gradient are plotted in Fig. 3.10(a) and Fig. 3.10(b), respectively.

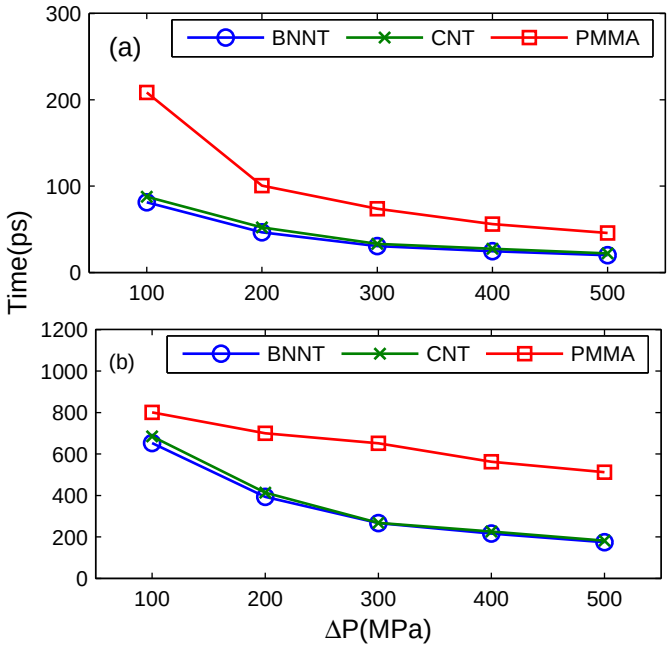

Figure 3.10: (a) Variation of the entrance time (T_e) and (b) translocation time (T_t) with the applied pressure gradient. T_t is approximately NT_e for BNNT and CNT where N is number of water molecules inside pore . In this study, $N = 8$.

In single-file water transport, for one water molecule to completely traverse the pore, an average number of water molecules, N, inside the pore should exit the pore. The calculated translocation time from the MD data is found to be $T_t \approx NT_e$ with $N = 8$ for BNNT and CNT. The entrance and translocation times in the PMMA case did not strictly obey this condition due to the occupation of more than single-file water at the pore entrance region. Both the translocation time and the entrance time are found to be the shortest in the BNNT pore, and the translocation time of water molecules through the PMMA pore is considerably longer. This is consistent with the results obtained for the water flux.

3.4 Conclusion

To conclude, RO through three different membranes made of BNNT, CNT and PMMA pores was compared by non-equilibrium MD simulation. By applying high pressure, the water molecules transported from 4 M KCl solution to pure water against the osmotic potential gradient while ions are perfectly rejected with an average pore diameter of 0.82 nm. Simulation results indicated that the water flux is significantly higher for BNNT and CNT compared to PMMA, and slightly higher for BNNT compared to CNT. The water flux was three to four orders of magnitude higher than that estimated by the pore model. The solution-diffusion model also failed to explain the enhanced water flux for BNNT and CNT by neglecting the collective motion of water molecules.

The collective "hopping" mechanism was introduced to describe the water transport. Simulation result was in reasonable agreement with the theoretical model. Also, PMMA permeation coefficient was consistent with the experimentally measured permeation coefficient for aquaporin 1 water channel due to the structural similarity of polymer. PMF analysis indicated that smooth pore surface character contributes to an order of magnitude higher water flux for BNNT and CNT compared to PMMA. Slightly higher permeation coefficient for BNNT was explained by stronger Van der Waals interaction between BNNT and water

compared to CNT. Our results suggest that future RO membrane design could incorporate BNNT and CNT for energy efficient water filtration, desalination, bio-seperation, etc.

Chapter 4

Enhanced reverse osmosis by inducing an electric field

4.1 Introduction

In a previous chapter, we focused on seeking energy efficient membranes which can be used for low cost reverse-osmosis process. It was found that water flux through BNNT and CNT are higher compared to PMMA membrane and can be used for future reverse osmosis process. In addition to the type of the membrane used, several other factors can affect water flux and controlling these can lead to efficient membrane separation technology. Raghunathan and Aluru showed that osmotic water flux through a negatively charged pore is higher compared to the osmotic water flux in a positively charged pore followed by the osmotic water flux in the uncharged pore [45]. They also showed that osmotic water flux depends on the size-asymmetric property of electrolytes due to a differential cation and anion affinity [59]. Gong et al. [60] showed that an asymmetric charge arrangement on the pore can pump water in one direction as fast as 4.4 water molecules/ns due to an asymmetrical potential between the two ends of the pore. Effect of electric field on fluids confined in the nanopore has been studied by Dzubiella et al. [61]. They induced an electric field by imbalance of net charges of ions in the reservoirs. Induced electric field contributed to wetting of hydrophobic nanopore by coupled transport of water and ions. After ion permeations, induced electric field vanishes, and nanopore stops conducting water and ions, demonstrating voltage gating of ion channel. Vaitheeswaran et al. studied the effect of electric field on single-file water molecules confined in (6,6) nonpolar CNT using Monte Carlo simulation [62]. They observed that dipole orientation of single-file water molecules depends on the direction of the electric

field.

Recently, it was shown that dipole orientation of water molecules confined in nanoscale tube can induce net water flux in the direction of dipole vector without any external driving force, and this phenomenon was explained by rotational-translation coupling of water molecules [63]. In this paper, we investigate the effect of electric field induced across an RO membrane on dipole orientation of water molecules and on the RO water flux. Simulation results indicate that water flux is higher when dipole vector is in the direction of RO compared to the water flux when the dipole vector is in the opposite direction of RO.

4.2 Electric field induced by biomolecules

Oppositely charged biomolecules were contained in a solution chamber and a pure water chamber to induce an electric-field. Amino acids, "building blocks" of proteins, were selected since they are large enough not to transport through reverse-osmosis membranes and small enough not to require large system size. Fig. 4.1 describes the general structure of amino acids with the amino group and the carboxyl group. Side chain represented by R determines the types of amino acids. In an aqueous solution, the amino group can be protonated and the carboxyl group can be deprotonated depending on pH. This ionized carboxyl group and amino group carries a positive charge and a negarive charge, respectively, but the molecule is neutral and called zwitterion.

We used lysine and aspartic acid carrying a positive charge and a negative charge at neutral, respectively. Their chemical structures are shown in Fig. 4.2. LJ parameters and partial charges are taken from updated Gromos96 force-field for improved hydration free enthalpy [64]. To induce electric-field in direction of RO (+z-direction), we put one lysine molecule in solution chamber and one aspartic acid molecule in pure water chamber. To induce electric-field in the direction opposite to RO (-z-direction), we put one lysine molecule in the pure water chamber and one aspartic acid molecule in the solution chamber. Since no

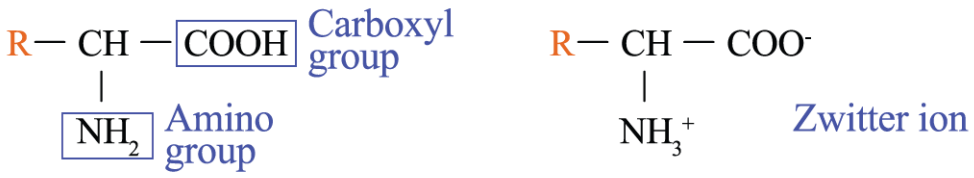

Figure 4.1: Chemical structure of amino acids composed of side chain, R, amino group and carboxyl group. Left describes zwitterion form.

ions permeate through the nanopore, induced electric-field is maintained during the course of the simulation.

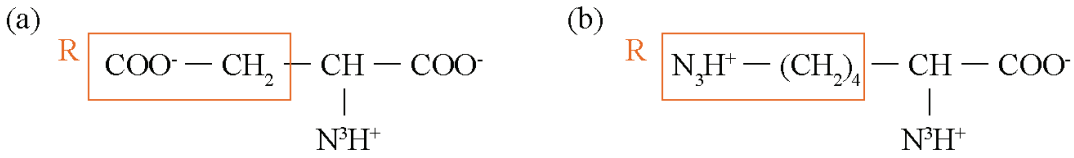

Figure 4.2: Chemical structure of (a)aspartic acid and (b)lysine. At pH7, net charges of aspartic acid and lysine are -1e and +1e, respectively.

BNNT membrane, which was introduced in chapter 3 was used in this study since the electric-field screening effect of BNNT is negligible compared to CNT due to the wide band gap (∼5.5 eV) of BNNT. Guo et al. [65] performed *ab initio* investigations of full static dielectric response of BNNT. Calculated axial permittivity of (6,6) BNNT based on the theory developed by Guo et al. is 6.5. Due to electrostatic attraction, amino acids are found near the membrane wall. Thus, the estimates of induced field strength inside the pore can be calculated by assuming two charged slabs enclosing a medium with permittivity, ϵ_m and a pore with permittivity, ϵ_p [66]. The calculated electric field strength at the center of the pore is 1.1 V/nm assuming BNNT is non-polar ($\epsilon_p = 1$) and screened electric-field strength due to pore permittivity of BNNT ($\epsilon_p = 6.5$) is 1.03 V/nm. Since the screening effect of

BNNT is small, we will assume that BNNT is non-polar in the calculations presented below.

4.3 Results and analysis

Water flux comparison

Simulations were performed without an induced electric-field, and with a positive and negative induced electric field. Water flux for each ΔP case was calculated by dividing the total number of water molecules transported from the solution chamber to the pure water chamber by the total simulation time. Water flux varies linearly with the applied ΔP as expected from irreversible thermodynamics model. As reported earlier, linear behavior does not necessarily require a small pressure gradient [52] due to an insignificant change in water configuration inside the pore. We observed a higher water flux for RO with a positive electric-field followed by the water flux with no electric field and with the negative electric field (see Fig. 4.3). Comparing the water flux obtained with the positive electric-field to that of the negative electric-field, the water flux difference is almost constant regardless of the external pressure gradient. The water flux obtained without any electric-field is in between the two electric-field cases. Continuum description of electrical body forces indicate the same effect of electric-field regardless of the electric-field direction. Thus, obtained water flux differences are not explained by continuum electrical body force.

Dipole orientation

The presence of an induced electric-field controls the dipole orientation of water molecules confined in the nanopore. As shown in the inset snapshot of Fig. 4.4, the dipole vectors of all the water molecules inside the (6,6) BNNT point in the same direction, either toward the solution reservoir or the pure water reservoir depending on the direction of the electric field. The water dipole vector is defined such that it points from the water oxygen to the center of mass of its hydrogen atoms. We averaged the angle between dipole vectors of water molecules inside the pore and the tube axis z at each sampling time, and they are

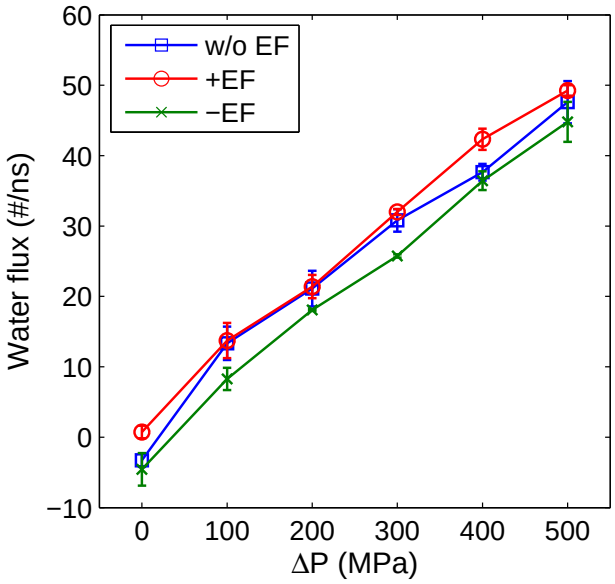

Figure 4.3: Variation of the RO water flux with the applied pressure gradient for BNNT without electric field (w/o EF), with positive electric field (+EF), and with negative electric field (-EF). Water flux with a positive electric field is higher compared to the water flux with negative electric field. Water flux without electric field is in between the two electric field cases. A negative water flux implies that the flow is from the pure water chamber to the solution chamber, which is due to osmosis of water.

plotted in Fig. 4.4. Water dipole vector points towards the pure water reservoir for positive electric-field (see Fig. 4.4(a)) and towards the solution reservoir for negative electric-field (see Fig. 4.4(b)). In the absence of an electric-field, dipole vectors of water molecules inside the (6,6) BNNT flip (see Fig. 4.4(c)).

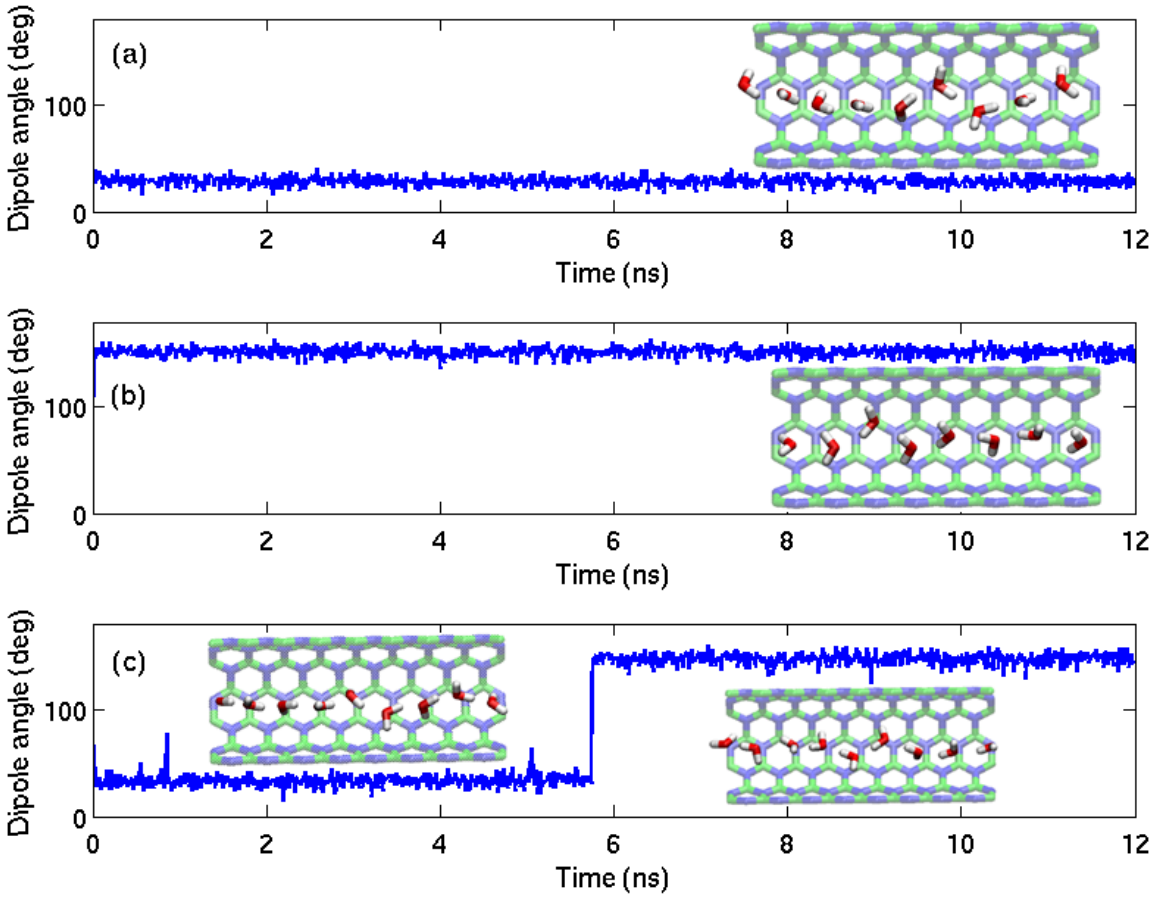

Figure 4.4: Averaged water dipole angle with time when (a) positive electric field (b) negative electric field, and (c) no electric field is induced. Applied pressure gradient is 300 MPa. The dipole angle is defined as the angle between water dipole vector and positive z axis. Dipole orientation angle is about 30° when a positive electric field is induced, and the dipole vector points toward pure water reservoir. The dipole orientation angle is about 150° when a negative electric field is induced, and the dipole vector points towards the solution reservoir.

The dipole time fraction of dipole vector pointing towards the pure water reservoir can be

calculated using $P_{+\text{dipole}} = T_{\theta<90}/T$ where $T_{\theta<90}$ is the total time when the dipole orientation angle, θ, is less than 90° and T is the total simulation time. Therefore, $P_{-\text{dipole}} = 1 - P_{+\text{dipole}}$. $P_{+\text{dipole}}$ for different pressure gradients is summarized in Table 4.1.

Table 4.1: Dipole orientation time fraction ($P_{+\text{dipole}}$) for RO simulation with positive electric field (+EF), negative electric field (-EF), and no electric field (w/o EF).

ΔP	+EF	-EF	w/o EF
0	1	0	0.59
100	1	0	0.82
200	1	0	0.55
300	1	0	0.55
400	1	0	0.44
500	1	0	1

For an equilibrium simulation with identical reservoirs connecting the pore, this value should be 0.5 if the simulation time is sufficiently long. For a reverse-osmosis simulation without an electric-field, the preference of the dipole angle is not clear. To understand the effect of dipole orientation on water flux, we separated the two different dipole states of RO simulation without an electric field, and calculated the water flux corresponding to each dipole state (see Fig. 4.5). +dipole denotes the water flux when the dipole vector points towards the pure water reservoir and -dipole denotes the water flux when the dipole vector points towards the solution reservoir. Fig. 4.5 shows that the water flux for +dipole state is always higher than that of the -dipole state. This indicates that a positive electric field, maintaining a +dipole state, gives the upper limit of water flux, while the negative electric field maintains the dipole vector pointing towards the solution reservoir, and gives the lower limit of water flux for a given pressure gradient.

Equilibrium simulation

To confirm the dependence of water flux on dipole orientation, an equilibrium simulation was performed without an electric-field, external pressure gradient and concentration gradient. Both reservoirs are filled with pure water, and simulation is run at 300 K using

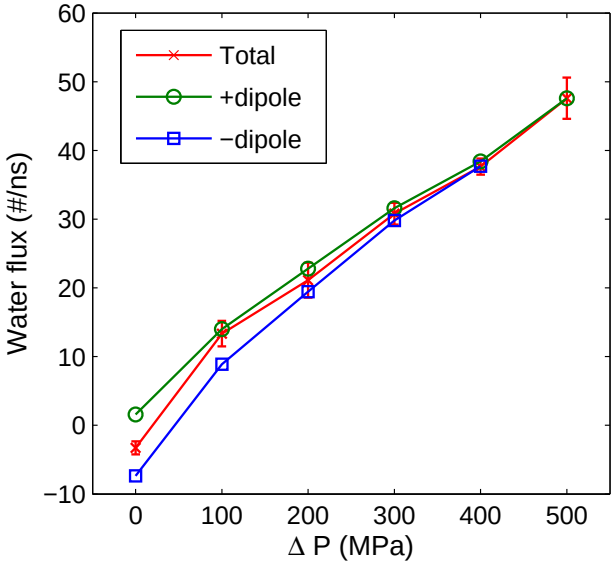

Figure 4.5: Water flux corresponding to each dipole state for RO simulation without electric field. +dipole denotes the water flux when the dipole vector points towards the pure water reservoir and -dipole denotes the water flux when the dipole vector points towards the solution reservoir. Total water flux is the water flux calculated for the entire time. Water flux for +dipole state is higher than that for the -dipole state. Total water flux depends on the dipole time fraction.

NVT ensemble for 20 ns. The cumulative water flux and the dipole orientation are plotted in Fig. 4.6(a) and Fig. 4.6(b), respectively. Although, there is fluctuation due to the high thermal velocity, water molecules are predominantly transported in the direction of dipole vector. From 0 to 8.52 ns, water dipole vector pointed to the left reservoir and water flux was about -2.99 water molecules/ns (calculated after 500 ps filling and initialization time). From 8.52 ns to 20 ns, water dipole vector pointed to the right reservoir, and water flux was about +2.96 water molecules/ns. The water flux difference between these two different states is 5.95 water molecules/ns, and it is close to the average water flux difference of 5.93 water molecules/ns between positive electric-field and negative electric-field in reverse osmosis simulation. The mechanism governing water translocation in the direction of the dipole vector has been explained recently by the rotation-translation coupling of water molecules confined in the nanopore [63].

We also examined the equilibrium potential of mean force (PMF) [67] when the dipole vector pointed to the left reservoir from 500 ps to 8.52 ns (see Fig. 4.6(c)). It is known that there is a significant energy barrier at the pore entrance [68, 40]. The energy barrier at the pore entrance interfacing left reservoir and right reservoir are 5.214 k_BT and 5.028 k_BT, respectively. They are measured at the first maxima from each end of the pore. This energy barrier difference (ΔE_b=-0.186 k_BT) also indicates preferred translocation direction from the right reservoir to the left reservoir since the permeation is more favorable into the lower energy barrier. Such a unidirectional water transport due to the asymmetric potential has been studied elsewhere [60]. The potential of mean force can be decomposed by integrating the force components by other water molecules or membrane molecules [69]. The decomposition indicates that the energy barrier difference is caused by the water-water interaction supporting the possible mechanism of rotation-translation coupling of water molecules [63].

Theoretical approach

Using the Kramer's theory and linear approximation, the net flux, $J = k^+ - k^- =$

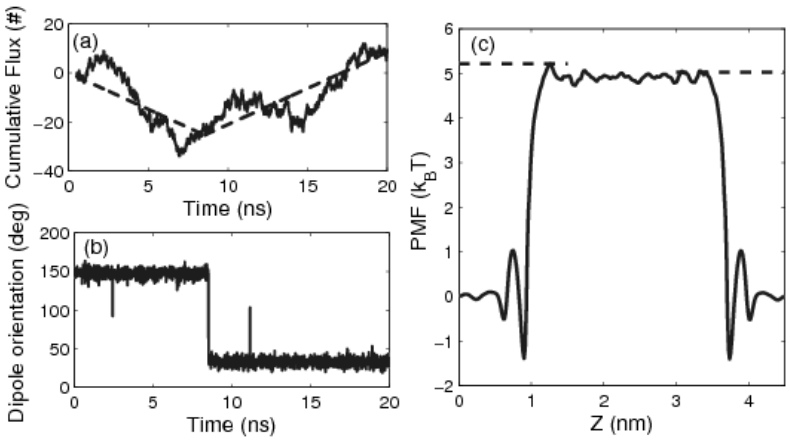

Figure 4.6: (a) Cumulative flux and (b) dipole orientation as a function of time for equilibrium simulation. Cumulative flux is calculated by counting water molecules translocated through the pore. Water molecules are added if they translocate from left to right reservoir and subtracted if they translocate from right to left reservoir. Average water flux is -2.99 #/ns (dashed line from 500 ps to 8.52 ns) when dipole vector points towards the left reservoir and +2.96 #/ns (dashed line from 8.52 ns to 20 ns) when dipole vector points towards the right reservoir. (c) Potential of mean force profile of water molecules when dipole orientation of water molecules is greater than 90°(from 500 ps to 8.52 ns). Energy barrier at the pore entrance is slightly smaller in the right compared to the left.

$k_0(\Delta E_b/k_BT)$ [70, 57] where k^+ is forward hopping rate, k^- is backward hopping rate and k_0 is bidirectional hopping rate, $(k^+ + k^-)/2$. When the dipole orientation is not preserved, $k_0 = k^+ = k^-$, and k_0 is the equilibrium hopping rate [71]. Substituting ΔE_b (-0.186 k_BT) and k_0 (16.0 ns^{-1}) [68], the calculated net flux is -2.98 water molecules/ns, which is close to the observed net flux (-2.99 water molecules/ns). When the chemical potential gradient, $\Delta\mu$, is applied across the pore for reverse osmosis, the total energy barrier difference across the pore corresponds to $\Delta\mu + \Delta E_b$. Then, the net water flux is given by $J = k_0(\Delta\mu/k_BT) + k_0(\Delta E_b/k_BT)$. The first term is the water flux due to the chemical potential gradient and the second term is the water flux due to the single-file dipole orientation. This equation supports the superimposition of the water flux driven by the chemical potential gradient, which is due to the pressure gradient and the concentration gradient, and water flux due to the single-file dipole orientation as a result of induced electric field.

We can also introduce an additional equilibrium constant, $c = k_0(\Delta E_b/k_BT)$. Considering the dipole time fraction, $P_{+dipole}$ as defined above, generalized net water flux is given by

$$J = k_0(\Delta\mu/k_BT) + c(2P_{+dipole} - 1) \tag{1}$$

where c=2.98 ns^{-1} and k_0 =16 ns^{-1}. When there is no preference on the dipole orientation, $P_{+dipole} = 0.5$ and $J = k_0(\Delta\mu/k_BT)$ as reported in other studies [52, 57, 70, 68]. The water flux obtained by MD simulation and equation (1) is compared in Fig. 4.7. $P_{+dipole}$ used in calculation is specified in Table 1. Assuming ideal solution and unity activity coefficient, the chemical potential gradient is calculated by integrating,

$$\mathrm{d}\mu = k_BT\ln x + v\mathrm{d}P/N_A \tag{2}$$

where x is the molar concentration of water, v is the molar volume, P is the pressure, and N_A is the Avogadro number. The water fluxes from the RO simulation with positive electric field and negative electric field are in reasonable agreement with equation (1) with $P_{+dipole} = 1$

and $P_{+dipole} = 0$, respectively. The reason for the deviation at high pressure can be due to the assumption of ideal solution in calculating the chemical potential.

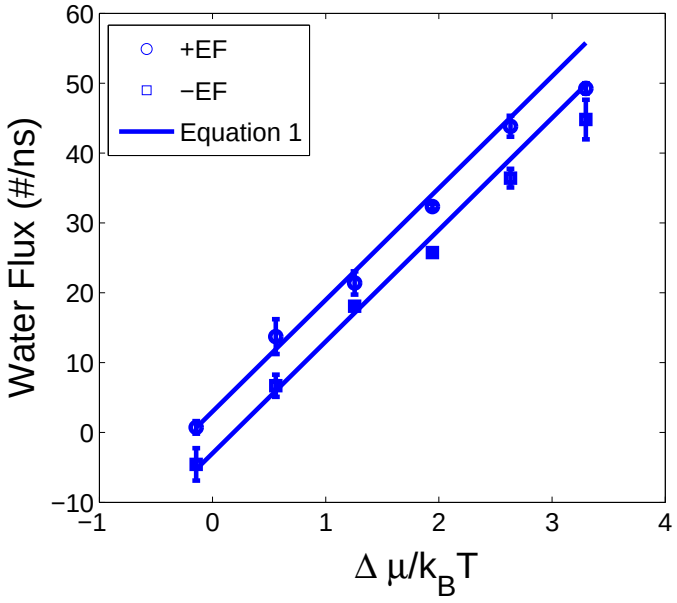

Figure 4.7: Comparison of water flux obtained from the MD simulation (+EF and -EF) with that predicted from equation (1). +EF and -EF denote RO water flux with positive electric field and negative electric field, respectively. The upper and lower solid line is calculated with $P_{+dipole} = 1$ and $P_{+dipole} = 0$, respectively.

Effect of partial charge

Won et al. [72, 42] showed that partial charges of (6,6) BNNT with a length of about 1.4 nm flipped the dipole orientation of water at the center of the pore, which resulted in the formation of L-defect at the center of the pore. We introduced the partial charges to investigate its effect on the RO water flux. We tested the BNNT saturated at the ends with hydrogen atoms to use the partial charges reported by Won et al. [72]. Induced electric field still maintained the dipole vector of water molecules in the direction of the electric field, and we observed insignificant change of water flux when partial charges are introduced. With 300 MPa of pressure gradient and electric field induced in the positive z-direction, the water

flux without partial charges and with partial charges was 37.7 water molecules/ns and 37.9 water molecules/ns, respectively. When electric field is induced in the negative z-direction, the water flux without partial charges and with partial charges was 32.3 water molecules/ns and 34.3 water molecules/ns, respectively. The water flux through hydrogen terminated BNNT was about 6 water molecules/ns higher compared to that through naked BNNT due to the hydrophilicity at the pore entrance [68, 73].

In a prior study on reverse osmosis, it was observed that with ions as solutes the reverse osmosis flux through model membranes made of spherical LJ atoms and thin zeolite membranes was enhanced when periodically reversed electric field was applied [74, 47, 75, 76]. When a static electric field was applied, reverse osmosis flux did not increase as ions permeated through the pore and clogged the pore. In addition, molecular orientation effects on reverse osmosis flux were not observed [75]. However, the results in this study indicate that in the case of single-file water molecules confined inside a nanotube, molecular orientation can play an important role and have a significant effect on reverse osmosis.

4.4 Conclusion

We investigated the effect of induced electric field by biomolecules on reverse osmosis. It was found that electric field induced in the direction of RO enhanced RO water flux and in the direction opposite of RO suppressed it. This result was explained based on the dipole orientation of water molecules confined in (6,6) BNNT. Water molecules in (6,6) BNNT formed single-file and their concerted dipole vectors pointed either toward the positive or negative axial direction of BNNT. In equilibrium MD simulation, we also observed net motion of single-file water molecules in the direction of dipole vectors. Consequently, induced electric field constantly maintained the dipole vector in the direction of electric field, and around 3 water molecules/ns of water flux driven by dipole vector was superimposed on the pressure driven water flux of RO. Without an external pressure gradient, induced electric field in the

direction of RO generated about 0.73 water molecules/ns of water flux against the osmotic potential corresponding to 4 M concentration gradient. For 1.12 M salt concentration of sea water, RO water flux close to about 2.7 water molecules/ns can be achieved without external pressure gradient. In summary, induced electric field can enhance RO water flux and can be used for energy efficient RO process.

Chapter 5

Conclusions

We studied reverse osmosis processes through nanotube-based membranes using MD simulations, in order to investigate energy efficient membrane separation processes such as water desalination. A brief overview of MD simulation was presented with implementation details of reverse osmosis simulations. We applied a pressure piston method to simulate pressure driven flow against chemical potential. Enhanced reverse osmosis was found by 1) using CNT and BNNT membranes and 2) inducing electric field using charged biomolecules.

Simulation results indicated that the water flux is significantly higher for BNNT and CNT compared to PMMA, and slightly higher for BNNT compared to CNT. The water flux was three to four orders of magnitude higher than that estimated by the pore model. The solution-diffusion model also failed to explain the enhanced water flux for BNNT and CNT by neglecting the collective motion of water molecules. The collective "hopping" mechanism was introduced to describe the water transport. Simulation result was in reasonable agreement with the theoretical model. PMF analysis indicated that smooth pore surface character contributes to an order of magnitude higher water flux for BNNT and CNT compared to PMMA. Slightly higher permeation coefficient for BNNT was explained by stronger Van der Waals interaction between BNNT and water compared to CNT.

It was found that electric field induced in the direction of RO enhanced RO water flux and in the direction opposite of RO suppressed it. This result was explained based on the dipole orientation of water molecules confined in (6,6) BNNT. Water molecules in (6,6) BNNT formed single-file and their concerted dipole vectors pointed either toward the positive or negative axial direction of BNNT. In equilibrium MD simulation, we also observed net

motion of single-file water molecules in the direction of dipole vectors. Consequently, induced electric field constantly maintained the dipole vector in the direction of electric field, and around 3 water molecules/ns of water flux driven by dipole vector was superimposed on the pressure driven water flux of RO.

References

[1] M. A. Shannon, P. W. Bohn, M. Elimelech, J. G. Georgiadis, B. J. Marinas, and A. M. Mayes, *Nature* **452**, 301 (2008).

[2] D. V. der Spoel, E. Lindahl, B. Hess, A. R. van Buuren, E. Apol, P. J. Meulenhoff, D. P. Tieleman, A. L. Sijbers, K. A. Feenstra, and R. van Drunen H. J.C. Berendsen, *GROMACS user manual*, The GROMACS development team.

[3] D. Frenkel and B. Smit, *Understandings Molecular simulation*, Academic press, 2002.

[4] J. W. Eastwood and R. W. Hockney, *J. Comp. Phys.* **15**, 342 (1974).

[5] L. Greengard and V. Rokhlin, *J. Comp. Phys.* **73**, 325 (1987).

[6] M. Sangester and M. Dixon, *Adv. Phys.* **25**, 247 (1976).

[7] I. Yeh and M. Berkowitz, *J. Chem. Phys.* **111**, 7 (1999).

[8] E. Spohr, *J. Chem. Phys.* **107**, 6342 (1997).

[9] P. H. Hünenberger, *Adv. Polym. Sci.* **173**, 105 (2005).

[10] H. J. C. Berendsen, J. P. M. Postma, W. F. Gunsteren, A. DiNolar, and J. R. Haak, *J. Chem. Phys.* **81**, 3684 (1984).

[11] T. Morishita, *J. Chem. Phys.* **113**, 2976 (2000).

[12] S. Nose, *J. Chem. Phys.* **81**, 511 (1984).

[13] J. Ryckaert, G. Ciccotti, and H. Berendsen, *J. Comp. Phys.* **23**, 327 (1977).

[14] B. Hess, H. Bekker, and H. B. J. Fraaije, *J. Comp. Phys.* **18** (1997).

[15] H. C. Anderson, *J. Chem. Phys.* **52**, 24 (1983).

[16] S. Miyamoto and P. Kollman, *J. Comp. Chem.* **13**, 952 (1992).

[17] G. Karniadakis, A. Beskok, and N. Aluru, *Microflows and Nanoflows: Fundamentals and Simulation*, volume 29 of *Interdisciplinary Applied Mathematics*, Springer, 233 Spring Street, New York, NY 10013, USA, 2005.

[18] A. V. Raghunathan, Master's thesis, University of Illinois, 2005.

[19] H. Berendsen, J. Postma, W. F. van Gunsteren, and J. Hermans, *Intermolecular Forces*, reidel Dordrecht, 1981.

[20] M. W. Mahoney and W. L. Jorgensen, *J. Chem. Phys.* **12**, 8910 (2000).

[21] W. L. Jorgensen, J. Chandrasekhar, J. D. Madura, R. W. Impey, and M. L. Klein, *J. Chem. Phys.* **79**, 925 (1983).

[22] W. L. Jorgensen and J. D. Madura, *Mol. Phys.* **56**, 1381 (1985).

[23] Y. Liu and T. Ichiye, *J. Phys. Chem.* **100**, 2723 (1985).

[24] H. Berendsen, J. Grigera, and T. Straatsm, *J. Phys. Chem* **91**, 6269 (1987).

[25] F. H. Stillinger and A. Rahman, *J. Chem. Phys.* **60**, 1545 (1974).

[26] P. J. van Maaren and D. van der Spoel, *J. Phys. Chem. B* **105**, 2618 (2001).

[27] I. M. Svishchev, P. G. Kusalik, J. Wang, and R. Boyd, *J. Chem. Phys.* **105**, 4742 (1996).

[28] S. Koneshan, J. C. Rasaiah, R. M. Lynden-Bell, and S. H. Lee, *J. Phys. Chem. B* **102**, 4193 (1998).

[29] C. Huang, K. Nandakumar, P. Y. K. Choi, and L. W. Kostiuk, *J. Chem. Phys.* **124**, 234701 (2006).

[30] E. Lindahl, B. Hess, and D. van der Spoel, *J . Mol. Model.* **7**, 306 (2001).

[31] T. Darden, D. York, and L. Pedersen, *J. Chem. Phys.* **98**, 10089 (1993).

[32] W. Zhou and L. Song, **39**, 3382 (2005).

[33] M. L. Zeidel, S. V. Ambudkar, B. L. Smith, and P. Agre, *Biochemistry* **31**, 7436 (1992).

[34] S. Ghosh, A. K. Sood, and N. Kumar, *Science* **299**, 1042 (2003).

[35] J. H. Park, S. B. Sinnott, and N. R. Aluru, *Nanotechnology* , 895 (2006).

[36] B. Gao, *Chem. Phys. Lett.* **327**, 69 (2000).

[37] B. Q. Wei, R. Vajtai, and P. M. Ajayan, *Appl. Phys. Lett.* **79**, 1172 (2001).

[38] G. Hummer, J. G. Rasaiah, and J. P. Noworyta, *Nature* **414**, 188 (2001).

[39] A. Kalra, S. Garde, and G. Hummmer, *Proc. Natl. Acad. Sci. U.S.A.* **100**, 10175 (2003).

[40] C. Y. Won, S. Joseph, and N. R. Aluru, *J. Chem. Phys.* **125**, 114701 (2006).

[41] J. K. Holt, H. G. Park, Y. Wang, M. Stadermann, A. B. Artyukhin, C. P. Grigoropoulos, A. Noy, and O. Bakajin, *Science* **312**, 1034 (2006).

[42] C. Y. Won and N. R. Aluru, *J. Am. Chem. Soc.* **129**, 2748 (2007).

[43] J. Koplik, J. R. Banavar, and J. F. Willemsen, *Phys. Rev. Lett.* **60**, 1282 (1988).

[44] D. J. Evans and G. P. Morriss, *Phys. Rev. Lett.* **51**, 1776 (1983).

[45] A. V. Raghunathan and N. R. Aluru, *Phys. Rev. Lett.* **97**, 024501 (2006).

[46] R. Qiao and N. R. Aluru, *J. Chem. Phys.* **118**, 4692 (2003).

[47] S. Murad, K. Oder, and J. Lin, *Mol. Phys.* **95**, 401 (1998).

[48] J. Lin and S. Murad, *Mol. Phys.* **99**, 1175 (2001).

[49] L. Wirtz and A. Rubio, *Phys. Rev. B.* **68**, 045325 (2003).

[50] J. W. Kang and H. J. Hwang, *J. Phys.: Condens. Matter* **16**, 3901 (2004).

[51] G. Chen, Y. Guo, N. Karasawa, and W. A. Goddard, *Phys. Rev. B* **48**, 13959 (1993).

[52] F. Zhu, E. Tajkhorshid, and K. Schulten, *Phys. Rev. Lett.* **93**, 224501 (2004).

[53] J. G. Wijmans and R. W. Baker, *J. membrane Sci.* **107**, 1 (1995).

[54] H. C. Longuett-higgins and G. Austin, *Biophys. J.* **6**, 217 (1966).

[55] H. Lonsdale, U. Merten, and R. Riley, *J. Appl. Polym. Sci.* **9**, 1341 (1965).

[56] G. Jonsson and C. E. Boesen, *Desalination* **17**, 145 (1975).

[57] B. L. de Groot, D. P. Tieleman, P. Pohl, and H. Grubmüller, *Biophys. J.* **82**, 2934 (2002).

[58] G. Portella, P. Pohl, and B. L. de Groot, *Biophys. J.* **92**, 3930 (2007).

[59] A. V. Raghunathan and N. R. Aluru, *Appl. Phys. Lett.* **89**, 064107 (2006).

[60] X. Gong, J. Li, H. Lu, R. Wan, J. Li, J. Hu, and H. Fang, *Nat. Nanotechnol.* **2**, 709 (2007).

[61] J. Dzubiella, R. J. Allen, and J. P. Hansen, *J. Chem. Phys.* **120**, 5001 (2004).

[62] S. Vaitheeswaran, J. C. Rasaiah, and G. Hummer, *J. Chem. Phys.* **121**, 7955 (2004).

[63] S. Joseph and N. Aluru, *Phys. Rev. Lett.* **101**, 064502 (2008).

[64] C. Oostenbrink, A. Villa, A. E. Mark, and W. F. V. Gunsteren, *J. Comp. Chem.* **25**, 1656 (2004).

[65] G. Y. Guo, S. Ishibashi, T. Tamura, and K. Terakura, *Phys. Rev. B* **75**, 245403 (2007).

[66] J. Dzubiella and J. P. Hansen, *J. Chem. Phys.* **122**, 234706 (2005).

[67] R. Kjellander and H. Greberg, *J. Electroanal. Chem.* **450**, 233 (1998).

[68] M. E. Suk, A. Raghunathan, and N. R. Aluru, *Appl. Phys. Lett.* **92**, 133120 (2008).

[69] B. Roux and M. Karplus, *Biophys. J.* **59**, 961 (1991).

[70] B. L. de Groot and H. Grubmuller, *curr. Opin. Struct. Biol.* **15**, 176 (2005).

[71] A. Berezhkovskii and G. Hummer, *Phys. Rev. Lett.* **89**, 064503 (2002).

[72] C. Y. Won and N. R. Aluru, *J. Phys. Chem. C* **112**, 1812 (2008).

[73] J. Zheng, E. M. Lennon, H. Tsao, Y. Sheng, and S. Jiang, *J. Chem. Phys.* **122**, 214702 (2005).

[74] S. Murad and R. M. J. G. Powles, *Mol. Phys.* **90**, 671 (1997).

[75] R. Madhusuan, J. Lin, and S. Murad, *Fluid Phase Equilib.* **150**, 97 (1998).

[76] H. Yan, S. Murad, and E. Enciso, *Fluid Phase Equil.* **183**, 279 (2001).